AD-A112 805 MCDONNELL AIRCRAFT CO ST LOUIS MO F/G 11/6
INFLUENCE OF RARE-EARTH ADDITIONS ON PROPERTIES OF TITANIUM ALL--ETC(U)
AUG 80 S M SASTRY, R J LEDERICH, P S PAO N00014-76-C-0626
UNCLASSIFIED MDC-Q0718 NL

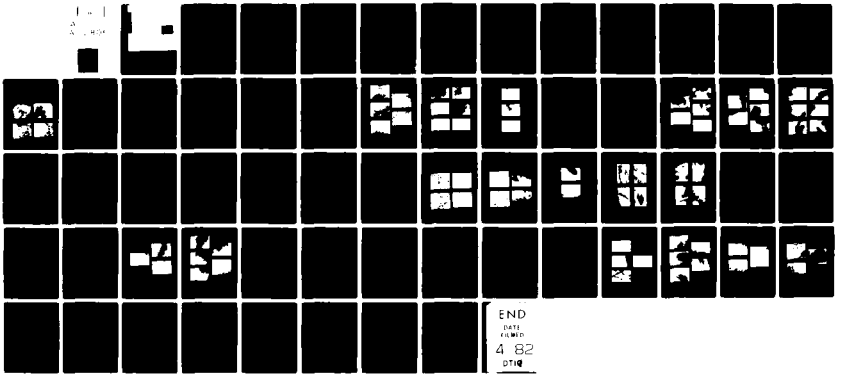

END
DATE FILMED
4 82
DTIC

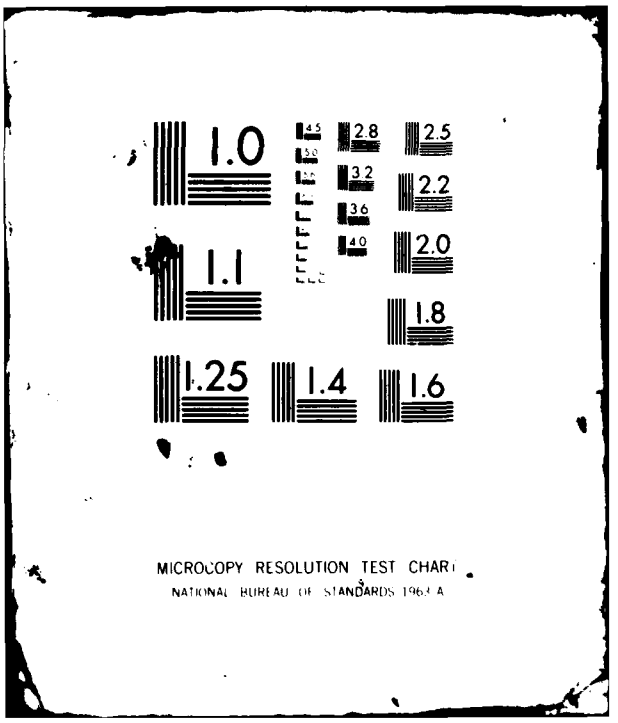
1.0
1.1
1.25
1.4
1.6
1.8
2.0
2.2
2.5
2.8
3.2
3.6
4.0
4.5
5.0
MICROCOPY RESOLUTION TEST CHART
NATIONAL BUREAU OF STANDARDS 1963 A

MCDONNELL DOUGLAS RESEARCH LABORATORIES

MCDONNELL DOUGLAS CORPORATION

UNCLASSIFIED

SECURITY CLASSIFICATION OF THIS PAGE *(When Data Entered)*

REPORT DOCUMENTATION PAGE		READ INSTRUCTIONS BEFORE COMPLETING FORM
1. REPORT NUMBER MDC Q0718	2. GOVT ACCESSION NO.	3. RECIPIENT'S CATALOG NUMBER
4. TITLE *(and Subtitle)* INFLUENCE OF RARE-EARTH ADDITIONS ON PROPERTIES OF TITANIUM ALLOYS - Effects of Yttrium and Erbium Additions on Ti-8Al and Ti-10Al Alloy		5. TYPE OF REPORT & PERIOD COVERED Technical Report 1 April 79 - 31 August 80 6. PERFORMING ORG. REPORT NUMBER
7. AUTHOR*(s)* S. M. L. Sastry, R. J. Lederich, P. S. Pao and J. E. O'Neal		8. CONTRACT OR GRANT NUMBER*(s)* N00014-76-C-0626
9. PERFORMING ORGANIZATION NAME AND ADDRESS McDonnell Douglas Research Laboratories McDonnell Douglas Corporation St. Louis, MO 63166		10. PROGRAM ELEMENT, PROJECT, TASK AREA & WORK UNIT NUMBERS
11. CONTROLLING OFFICE NAME AND ADDRESS Office of Naval Research 800 N. Quincy Street Arlington, VA 22217		12. REPORT DATE 31 August 1980 13. NUMBER OF PAGES 59
14. MONITORING AGENCY NAME & ADDRESS*(if different from Controlling Office)*		15. SECURITY CLASS. *(of this report)* Unclassified 15a. DECLASSIFICATION/DOWNGRADING SCHEDULE

16. DISTRIBUTION STATEMENT *(of this Report)*
Approved for public release; distribution unlimited.
No secondary distribution of this report outside U.S. Government agencies without prior approval of ONR Code 471.

17. DISTRIBUTION STATEMENT *(of the abstract entered in Block 20, if different from Report)*

18. SUPPLEMENTARY NOTES

19. KEY WORDS *(Continue on reverse side if necessary and identify by block number)*

Titanium alloy	Microstructure	Yield stress
Ti-8Al	Grain refinement	Fracture toughness
Ti-10Al	Precipitation strengthening	Creep
Yttrium	Second-phase Dispersion	Fatigue
Erbium	Ductility	

20. ABSTRACT *(Continue on reverse side if necessary and identify by block number)*

The influence of additions of 0.05-1.0 wt% Y and 0.2-2.0 wt% Er on the microstructure, slip distribution, fracture modes, and room- and elevated-temperature mechanical properties of Ti-8Al and Ti-10Al alloys was studied. Additions of up to 0.1 wt% Y and 0.2 wt% Er result in 50-200 nm incoherent dispersoids which effect grain refinement, reduce the planarity of slip, and significantly increase the ductility of Ti-8Al alloys. The additions further improve the room-temperature fracture toughness and room- and elevated-temperature low-cycle fatigue life of Ti-8Al and do not significantly alter the creep of

DD FORM 1 JAN 73 1473 EDITION OF 1 NOV 65 IS OBSOLETE

UNCLASSIFIED

SECURITY CLASSIFICATION OF THIS PAGE *(When Data Entered)*

Ti-8Al and Ti-10Al alloys. Higher amounts of Y and Er additions produce large, 1-5 μm dispersoids and produce no significant grain refinement or improvements in strength and ductility of the alloys.

micum

PREFACE

This report represents the results of the fourth phase of an investigation of the effects of rare-earth additives on titanium alloys performed by the McDonnell Douglas Research Laboratories under Office of Naval Research contract No. N00014-76-C-0626. The scientific officer for the contract is Dr. Bruce A. MacDonald of ONR.

The principal investigator is Dr. Shankar M. L. Sastry; co-investigators are Mr. Richard J. Lederich, Dr. Peter S. Pao, and Mr. James E. O'Neal. The work was performed in the Solid State Sciences department under the direction of Dr. Charles R. Whitsett.

This report has been reviewed and is approved.

Charles R. Whitsett
Chief Scientist - Solid State Sciences
McDonnell Douglas Research Laboratories

Donald P. Ames
Staff Vice President
McDonnell Douglas Research Laboratories

TABLE OF CONTENTS

LIST OF FIGURES

LIST OF TABLES

1. INTRODUCTION

A systematic investigation is being conducted of the effects of metallic rare-earth (RE) additions on the microstructure and properties of Ti alloys. In the first two years of this contract, the objective was to improve the high-temperature formability of Ti-6Al-4V, and it was determined that additions of 0.1 wt% Er or 0.05 wt% Y (1) improve the yield during initial forging of Ti-6Al-4V ingots, (2) reduce the high-temperature flow stress, (3) control grain size at β-processing temperatures, and (4) have no significant effect on yield strength and fracture toughness of α-β processed alloy (References 1-3).

The Widmanstätten microstructure of conventionally processed Ti-6Al-4V obscures the pronounced effects observed when rare-earths are added to α-Ti, and consequently, the research was shifted to α-rich and single-phase α alloys. Specifically, rare-earth-modified Ti-8Al and Ti-10Al, which have low density, high elastic modulus, high tensile strength, and high creep-resistance at 400-700°C, were investigated.

In titanium-aluminum alloys with aluminum concentrations between 10 and 20 at.%, the ordered and coherent α_2 phase (based on the composition Ti_3Al and having an ordered DO_{19} lattice structure) is precipitated upon aging (Figure 1) (References 4 and 5). Precipitation strengthening in these alloys is generally accompanied by a significant loss of ductility, which has been attributed to the formation of coarse planar-slip bands leading to stress concentrations at grain boundaries and slip-band intersections in the early stages of deformation. Plastic deformation in this type of alloy occurs by the shearing of α_2 precipitates by glide dislocations (References 6-8). However, the room- and elevated-temperature deformation behavior of this class of alloys and the possibility of improving the room-temperature ductility of the alloys have not been studied systematically.

The possibility of improving the room-temperature ductility of an α_2-precipitation-strengthened Ti-Al alloy by grain refinement has been demonstrated previously (Reference 9). A significant improvement in strength and ductility was observed in the alloy when the grain size was decreased from 90 μm to 9 μm (Figure 2). The increased strength results from the Hall-Petch

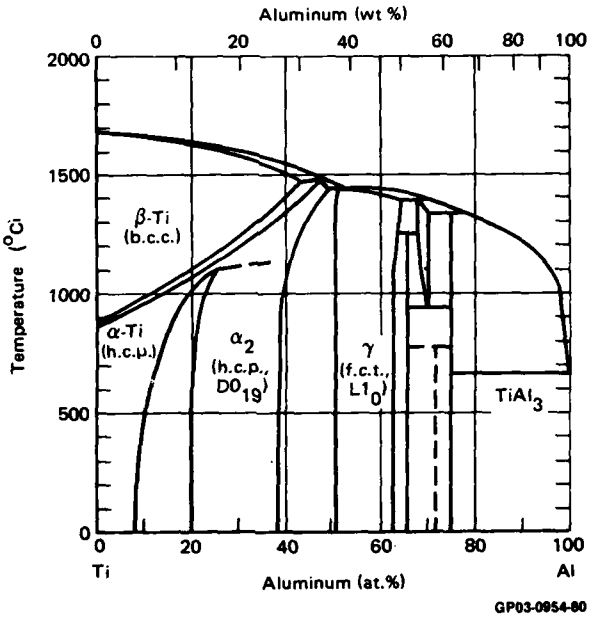

Figure 1. Phase diagram of the titanium-aluminum system.

grain-size dependence of flow stress. The improved ductility in fine-grained alloy results from a fine, homogeneous slip devoid of excessive localized stress-concentration sites (Figures 3 and 4).

Previous investigations at MDRL on the effects of rare-earth additions to pure titanium (References 10 and 11) have shown that the addition of small amounts of Er and Y to titanium results in a uniform dispersion of fine 20-50 nm diam particles in the metal matrix. The presence of such fine dispersoids results in a significant grain refinement and grain-growth retardation at elevated temperatures. These results demonstrate the potential beneficial effects of rare-earth additions to α_2-precipitation-strengthened Ti-Al alloys because both small grain size and the presence of fine dispersoids result in an increase in flow stress and are conducive to slip modification from coarse, planar slip to fine, uniformly dispersed slip. The dispersoids can act also as dislocation sources in a source-poor material.

For the fourth phase of this research program, the objectives were to:

(1) determine the influence of rare-earth dispersoids on recrystallization and grain-growth behavior in Ti-Al-RE alloys,

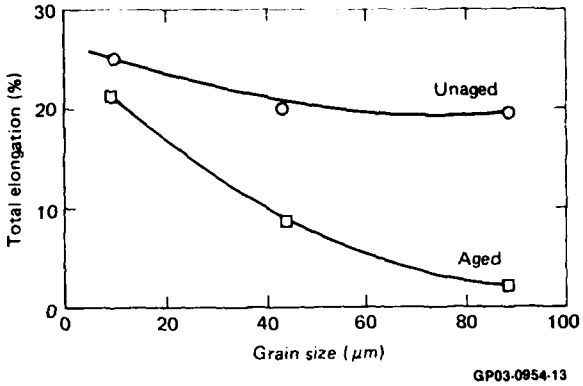

Figure 2. Effects of grain size and aging on ductility of Ti-8Al-0.25Si.

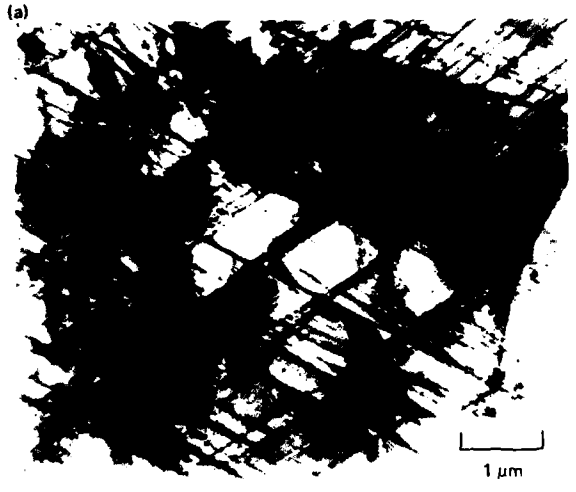

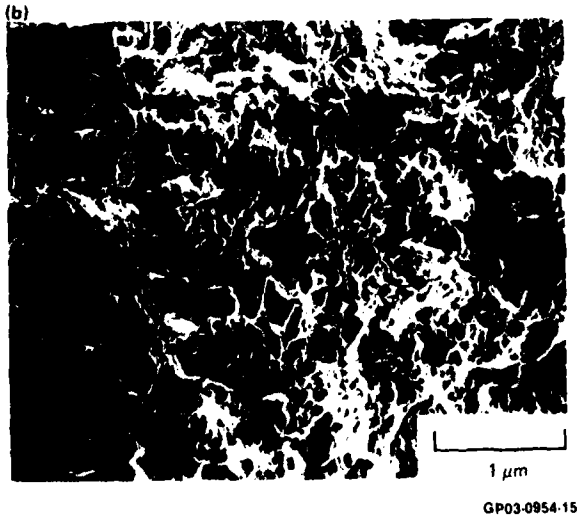

Figure 3. (a) Slip distribution and (b) fracture mode in Ti-8Al with 9-μm grain size.

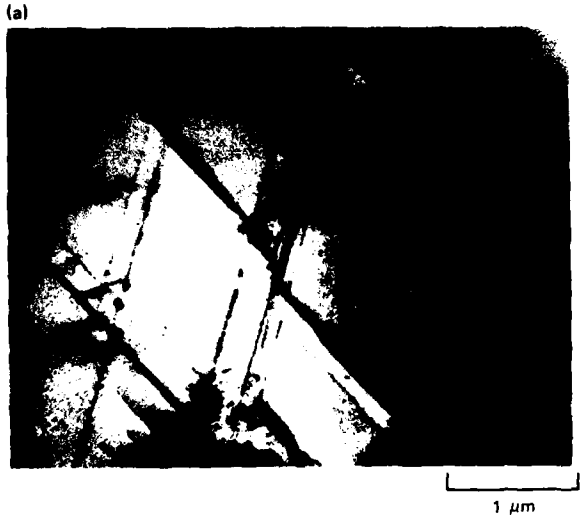

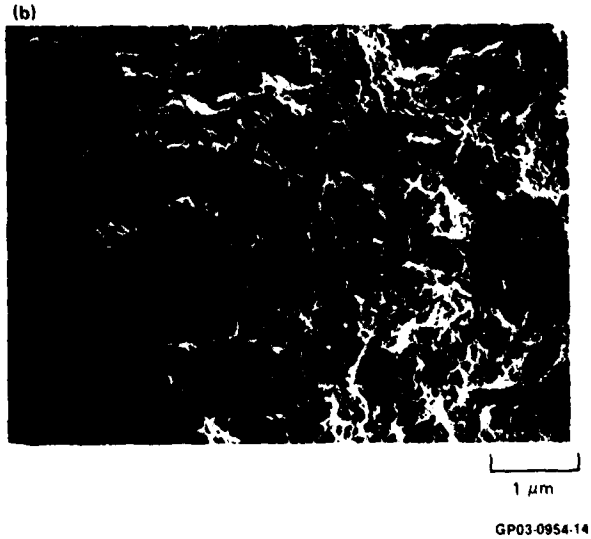

Figure 4. (a) Slip distribution and (b) fracture mode in Ti-8Al with 90-μm grain size.

(2) determine the influence of rare-earth dispersoids on room-temperature and elevated-temperature tensile properties of Ti-Al-RE alloys,

(3) determine the modification in slip behavior resulting from the combinations of rare-earth dispersoids and heat treatments,

(4) determine the high-temperature creep characteristics of Ti-Al-RE alloys,

(5) determine the room- and elevated-temperature, low-cycle fatigue characteristics of Ti-Al-RE alloys,

(6) determine the room-temperature fracture toughness of Ti-Al-RE alloys, and

(7) analyze the combined effects of α_2 precipitates and rare-earth dispersoids on the strength, ductility, and fracture toughness of Ti-Al alloys on the basis of microscopic mechanisms.

Figure 5 is an outline of the research on the effects of rare-earth additions on the microstructure and mechanical properties of Ti-8Al and Ti-10Al alloys.

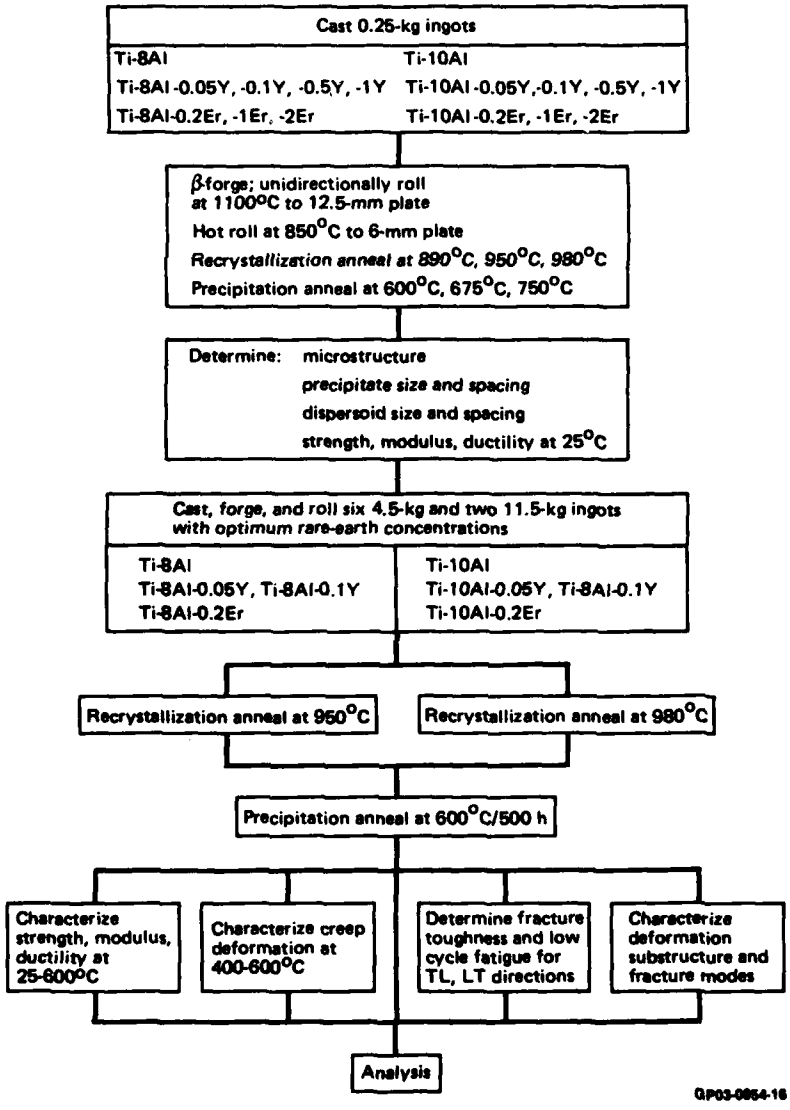

Figure 5. Outline of research on the effects of yttrium and erbium additions on the microstructure and mechanical properties of Ti-8Al and Ti-10Al alloys.

2. ALLOY PREPARATION AND PROCESSING

For preliminary assessment of the microstructural and mechanical-property changes effected by the addition of Er and Y, 0.25-kg button ingots of the alloy compositions shown in Table 1 were prepared by vacuum arc melting the alloys in a water-chilled copper hearth. Each button was prepared from a mixture of Ti-50A grade titanium, high-purity aluminum, and Ti-25Y and Ti-25Er master alloys. The button ingots were hot rolled to 3.5-mm sheets. The Ti-8Al-1.5Y, Ti-10Al-1.5Y, and Ti-10Al-2.0Er alloys cracked severely during rolling and could not be rolled to 3.5-mm sheets.

The alloy compositions shown in Table 2 were prepared at TIMET by consumable-electrode arc-melting 4.5-kg ingots in a purified dry-argon atmosphere using Ti-50A grade titanium, high-purity aluminum, and Ti-25Y and Ti-25Er master alloys. The ingots were forged and rolled at 1100°C to 12.5-mm plates, from which specimen blanks for fracture toughness determinations were cut. The 12.5-mm plates were then hot rolled at 850°C to 6-mm and 3-mm plates. Attempts to roll the alloys at a lower temperature to obtain heavily worked, unrecrystallized microstructures resulted in severe edge cracking of the alloys. Chemical analyses of samples taken from the ingots were performed by TIMET and revealed lower Er and Y concentrations than the aim chemistry (Table 2).

TABLE 1. COMPOSITIONS OF Ti-8Al-RE AND Ti-10Al-RE 0.25-kg BUTTON INGOTS.

Ti-8Al	Ti-10Al
Ti-8Al-0.05Y	Ti-10Al-0.05Y
Ti-8Al-0.10Y	Ti-10Al-0.10Y
Ti-8Al-0.50Y	Ti-10Al-0.50Y
Ti-8Al-1.00Y	Ti-10Al-1.00Y
Ti-8Al-0.2Er	Ti-10Al-0.2Er
Ti-8Al-1.0Er	Ti-10Al-1.0Er
Ti-8Al-2.0Er	Ti-10Al-2.0Er

GP03-0054-2

TABLE 2. COMPOSITIONS AND CHEMICAL ANALYSES OF Ti-8Al-RE AND Ti-10Al-RE 5-kg INGOTS.

Alloy heat no.	Nominal composition	Concentration (wt%)					
		Al	Fe	N	O	Y	Er
V5618	Ti-8Al	7.7	0.059	0.004	0.12	–	–
V5619	Ti-8Al-0.10Y	8.4	0.048	0.003	0.12	0.052	–
V5620	Ti-8Al-0.20Er	8.1	0.054	0.003	0.094	–	0.13
V5621	Ti-8Al-0.05Y	8.6	0.06	0.005	0.11	0.022	–
V5622	Ti-10Al	10.2	0.054	0.004	0.11	–	–
V5623	Ti-10Al-0.10Y	10.4	0.049	0.006	0.16	0.067	–
V5624	Ti-10Al-0.20Er	10.4	0.05	0.005	0.14	–	0.15
V5625	Ti-10Al-0.05Y	10.6	0.053	0.004	0.12	0.029	–

GP03-0854-3

3. MICROSTRUCTURAL CHARACTERIZATIONS

3.1 Microstructures of Hot-Rolled Ti-8Al-RE and Ti-10Al-RE Alloys

The rolled 6-mm and 12.5-mm alloy sheets had heavily worked, partially recrystallized grain structures, whereas the 3-mm sheets had fully recrystallized grains of 20 μm diameter. There were no significant differences between the as-rolled microstructures of the control and Y- and Er-containing alloys.

Figures 6 and 7 are thin-foil electron micrographs showing the dislocation substructures and dispersoids in the hot-rolled Ti-8Al-RE and Ti-10Al-RE alloys. The dispersoids in the Y- and Er-containing alloys are spherical, 50-200 nm in diameter, and incoherent with the matrix (Figures 6b, 6c, and 7b). Foils prepared from several alloys revealed that the density of dispersoids varied considerably within each alloy, and in some foils few dispersoids could be seen. The density of dispersoids in the thin foils was much lower than expected from the nominal rare-earth concentrations in the alloys. This result could be due to leaching of the dispersoids during electrolytic thinning of the foils or inhomogeneous mixing of the rare-earth additives during melting. In contrast with the fine dispersoids in the alloys containing less than 0.1 wt% Y or 0.2 wt% Er, the alloys containing higher Y and Er concentrations had numerous, coarse, 1-5 μm diameter, Y-rich and Er-rich particles. Figures 8-10 are scanning electron micrographs and x-ray spectra of the dispersoids observed in the alloys with high rare-earth concentrations.

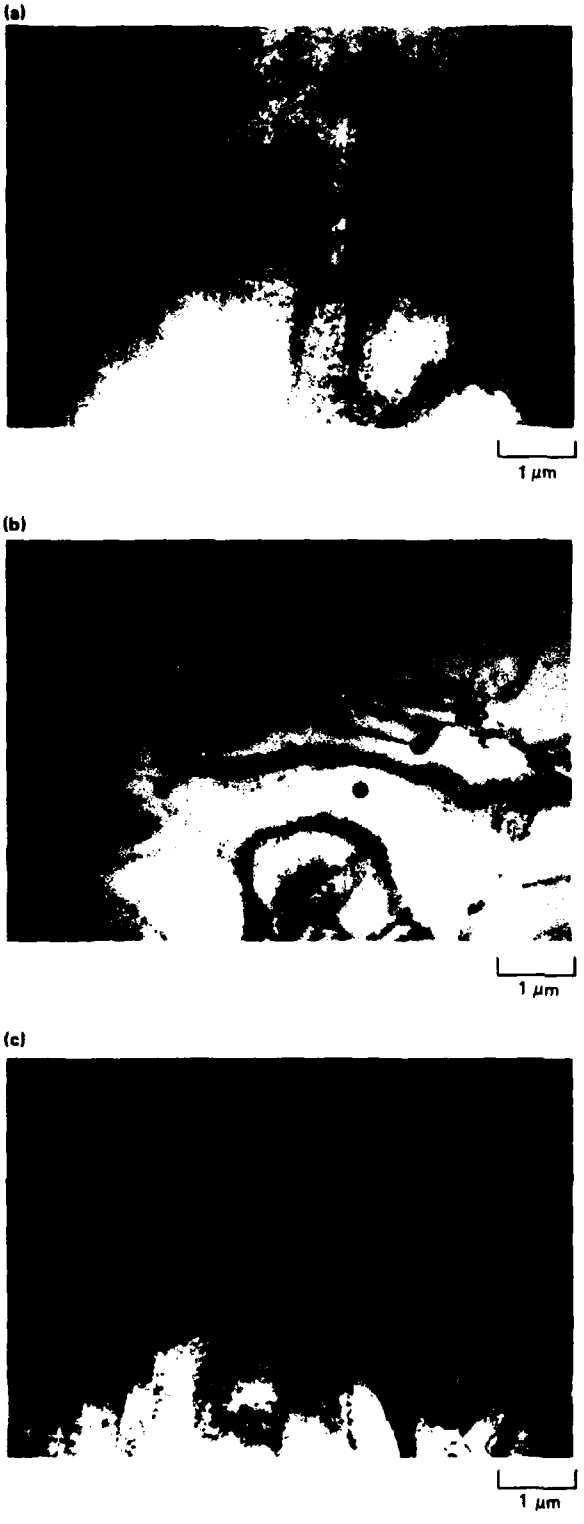

Figure 6. Transmission electron micrographs of hot-rolled (a) Ti-8Al, (b) Ti-8Al-0.1Y, and (c) Ti-8Al-0.2Er.

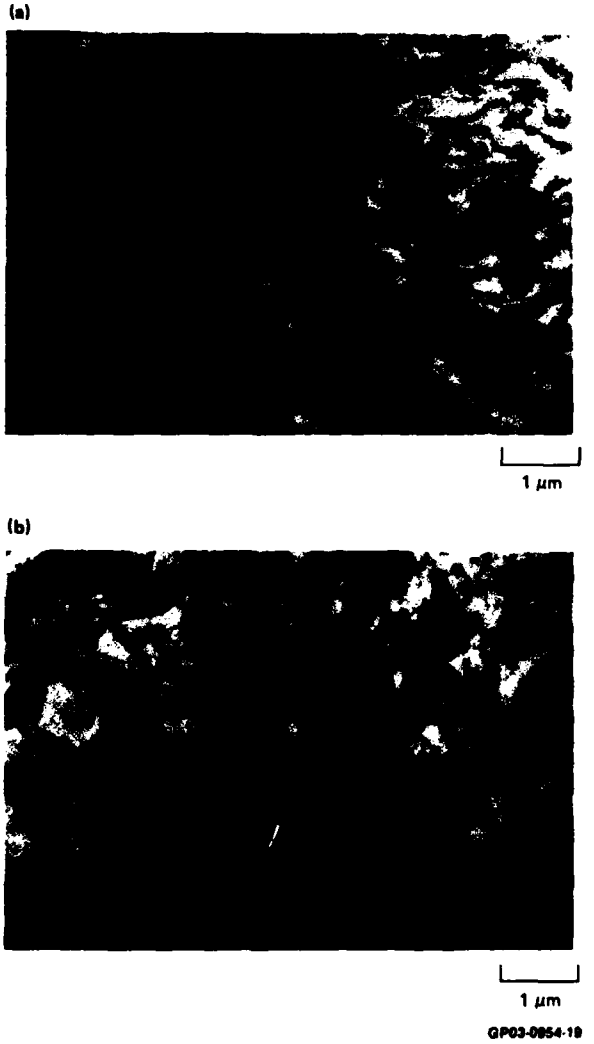

Figure 7. Transmission electron micrographs of hot-rolled **(a) Ti-10Al and (b) Ti-10Al-0.1Y alloys.**

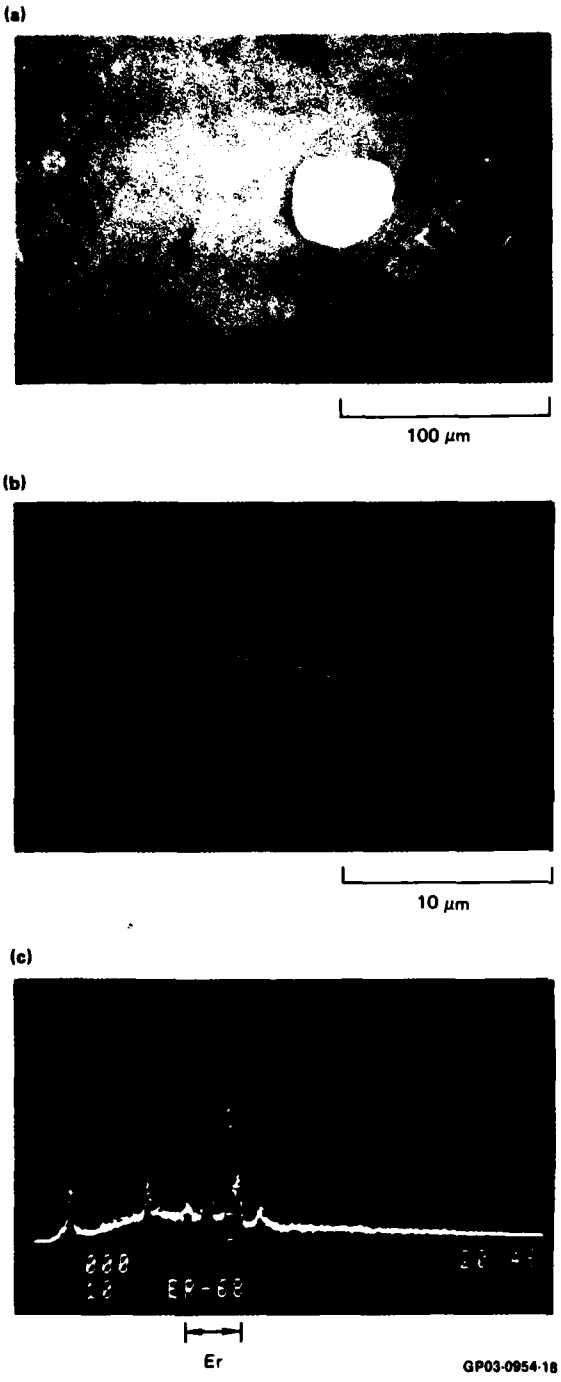

Figure 8. Scanning electron micrographs of Er dispersoids in Ti-8Al-1.0Er alloy: (a) and (b) secondary electron images of dispersoids, and (c) x-ray spectrum of the specimen.

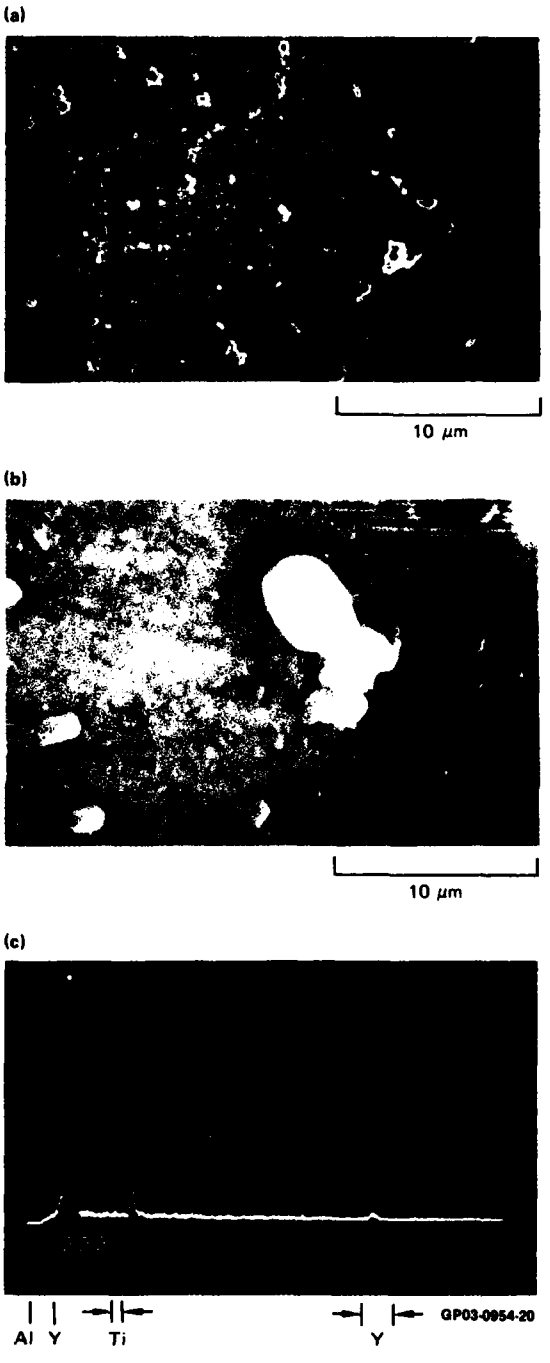

Figure 9. Scanning electron micrographs of Ti-10Al-1.5Y alloy: (a) and (b) secondary electron images of dispersoids, and (c) x-ray spectrum of the specimen.

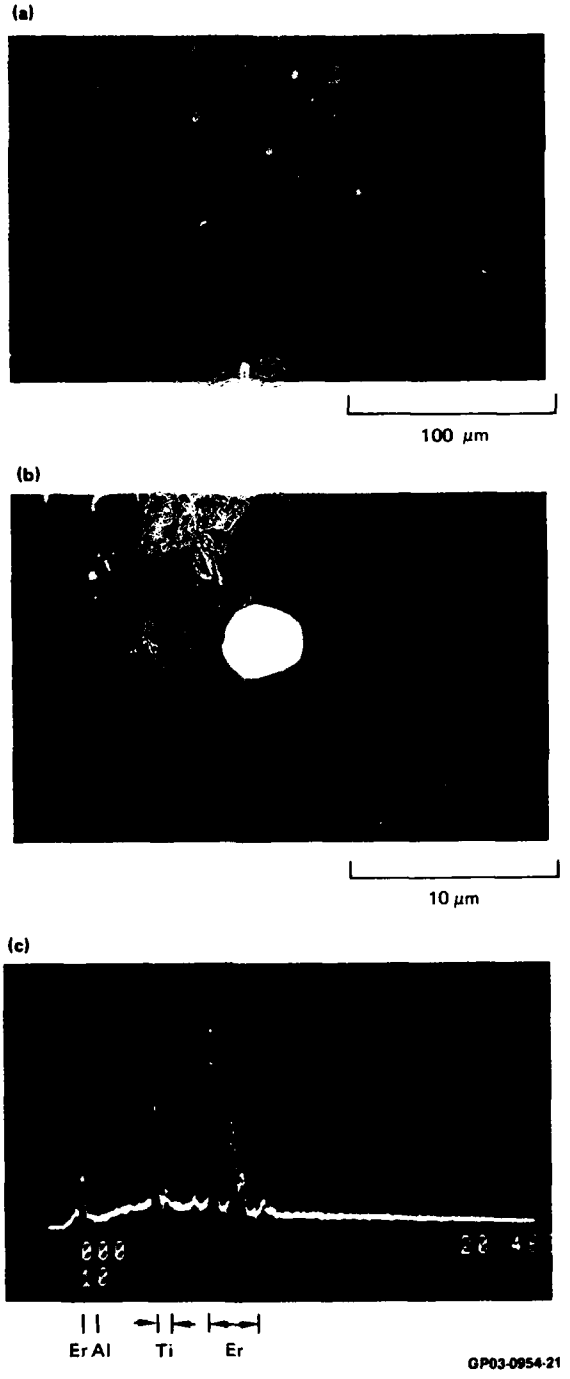

Figure 10. Scanning electron micrographs of Ti-10Al-2.0Er alloy: (a) and (b) secondary electron images of dispersoids, and (c) x-ray spectrum of the specimen.

3.2 Recrystallization and Grain-Growth of Ti-8Al-RE and Ti-10Al-RE Alloys

The hot-rolled Ti-8Al-RE and Ti-10Al-RE alloys were annealed at 890°, 920°, 950°, and 980°C and air cooled to room temperature to determine their recrystallization and grain-growth behavior. The grain sizes resulting from the different annealing treatments are shown in Table 3. For short, 10-min anneals at 890°, 920°, and 950°C, the grain size is unaffected by Er and Y, but for longer times, the rare-earth-containing alloys have smaller grain sizes than the control alloys. The grain refinement in Er- and Y-containing alloys results from an increased frequency of recrystallization nuclei and decreased rates of recrystallization and grain growth. The extent of grain refinement caused by each process depends on both the size and spacing of the second-phase particles; coarse (> 1 μm diam) particles increase the recrystallization nucleation frequency, and fine particles with an interparticle spacing less than 1 μm retard recrystallization and inhibit grain growth. The grain refinement effected by Er and Y additions is significantly less in Ti-8Al and Ti-10Al alloys than in pure Ti (References 10 and 11).

TABLE 3. EFFECTS OF ANNEALING TREATMENTS ON RECRYSTALLIZED GRAIN SIZE IN Ti-8Al-RE AND Ti-10Al-RE ALLOYS.

Annealing treatment*	Recrystallized grain size (μm)							
	Ti-8Al	Ti-8Al-0.05Y	Ti-8Al-0.10Y	Ti-8Al-0.20Er	Ti-10Al	Ti-10Al-0.05Y	Ti-10Al-0.10Y	Ti-10Al-0.20Er
As rolled	25.7	23.0	19.8	19.5	30.3	22.4	23.7	26.1
890°C/10 min/AC	12.6	–	15.4	–	–	–	–	–
920°C/10 min/AC	15.4	–	15.4	–	–	–	–	–
950°C/5 min/AC	15.6	–	16.2	–	–	–	–	–
900°C/1 h/AC	27.0	22.9	20.6	20.9	22.0	18.4	16.5	–
980°C/10 min/AC	24.0	23.9	24.3	23.9	–	–	–	–
950°C/10 min/AC 600°C/24 h/AC	31.9	26.2	18.8	23.2	–	–	–	–
980°C/6 min/AC	26.9	23.9	22.1	24.3	22.5	17.7	16.1	16.0
980°C/20 min/AC	28.2	–	30.9	–	–	–	–	–
980°C/10 min/AC 675°C/24 h/AC	41.3	30.5	24.9	25.8	–	–	–	–
980°C/1 h/AC	45.2	38.4	34.3	39.4	46.0	29.3	32.0	28.4
980°C/8 h/AC	44.1	–	28.2	28.6	–	–	–	–

*AC = air cooled

GP83-0864-4

3.3 Precipitation Behavior of Ti-8Al-RE and Ti-10Al-RE Alloys

To obtain variations in sizes and volume fractions of α_2-phase precipitate particles in the α-titanium matrix, precipitation anneals were performed at 750°C for 24 h and 600°C for 500 h for Ti-10Al-RE alloys quenched from 980°C and at 675°C for 24 h and 600°C for 500 h for Ti-8Al-RE alloys quenched from 950°C. Quenching from 950° and 980°C results in single-phase α as evidenced by an α-phase diffraction pattern without any α_2-precipitate reflections. Upon aging the alloys at 600°C for 500 h, the α_2-phase precipitates homogeneously in the form of elongated ellipsoids with their long directions parallel to the c-axis of the hexagonal matrix (Figures 11-13). The precipitate reflections are marked S in the selected area diffraction pattern shown in Figure 11b. The precipitates formed at 600°C are coherent with the matrix and are 5-10 nm in diameter as measured on the basal plane. The Y and Er additives have no effect on α_2 precipitation at 600°C. Upon aging the alloys at 675°C, however, the Ti-8Al-0.05Y has a single-phase α microstructure (Figure 14b), in contrast to the two-phase α + α_2 microstructure of Ti-8Al and Ti-8Al-0.2Er alloys (Figures 14a and 14c). The Y additions lower the α to α + α_2 transition temperature. The Ti-8Al-RE alloys aged at 750°C have single-phase α microstructures as shown in transmission electron micrographs and corresponding selected area diffraction patterns in Figure 15. The Ti-10Al-RE alloys aged at 750°C have two-phase α + α_2 microstructures (Figure 16).

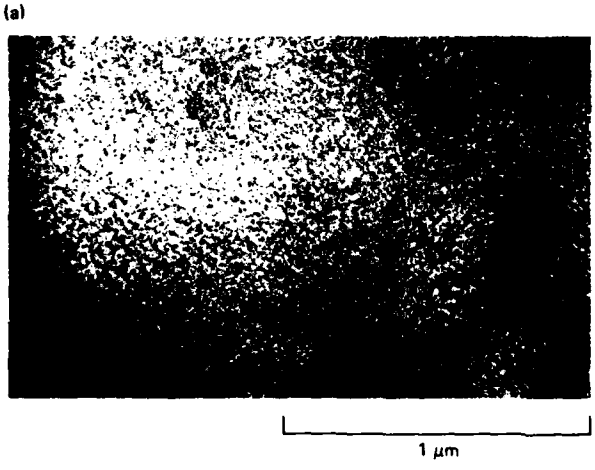

GP03-0954-22

Figure 11. Microstructure of Ti-8Al alloy aged at 600°C for 500 h and air cooled to 25°C: (a) bright-field transmission electron micrograph and (b) selected area diffraction (SAD) pattern.

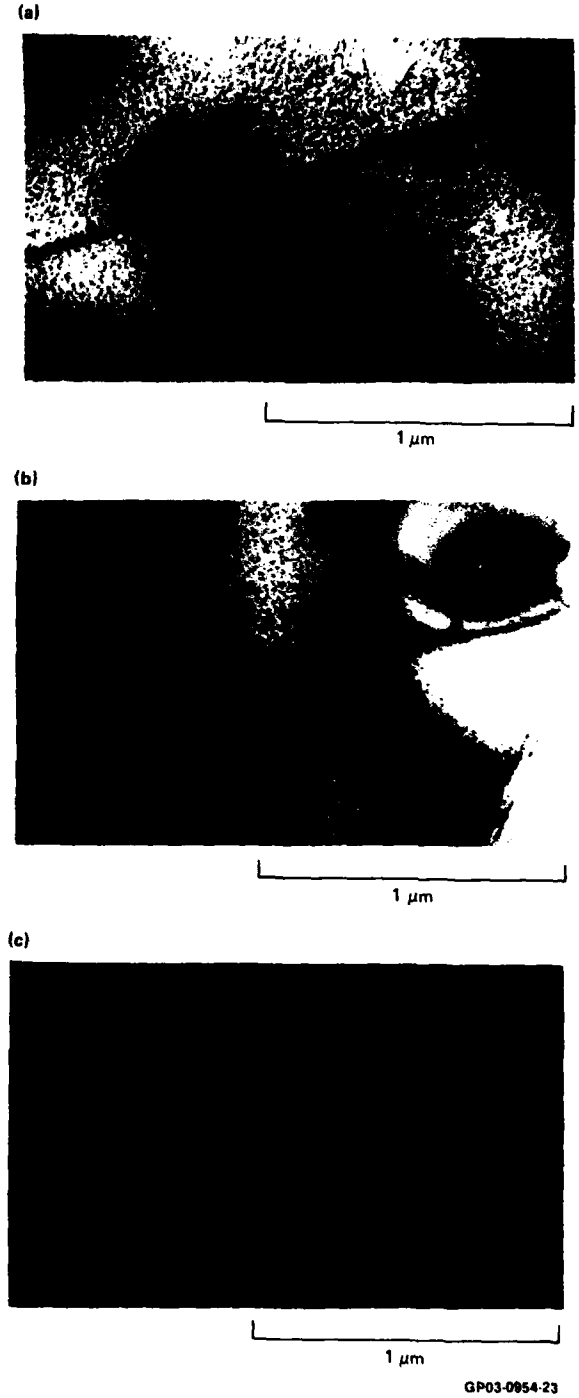

GP03-0954-23

Figure 12. Transmission electron micrographs of α_2 precipitates in (a) Ti-8Al, (b) Ti-8Al-0.1Y, and (c) Ti-8Al-0.2Er aged at 600°C for 500 h and air cooled to 25°C.

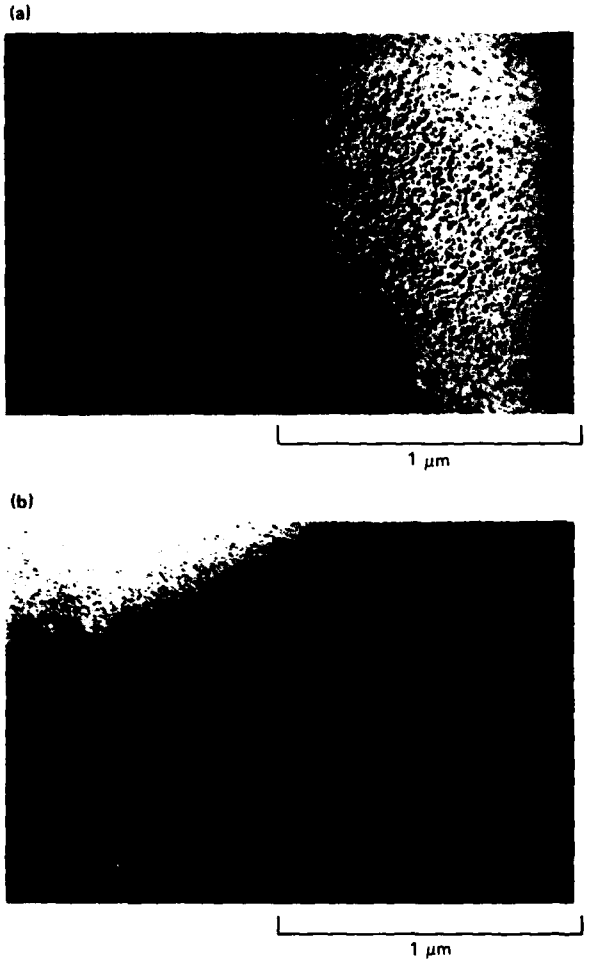

Figure 13. Transmission electron micrographs of (a) Ti-10Al and (b) Ti-10Al-0.1Y aged at 600°C for 500 h and air cooled to 25°C.

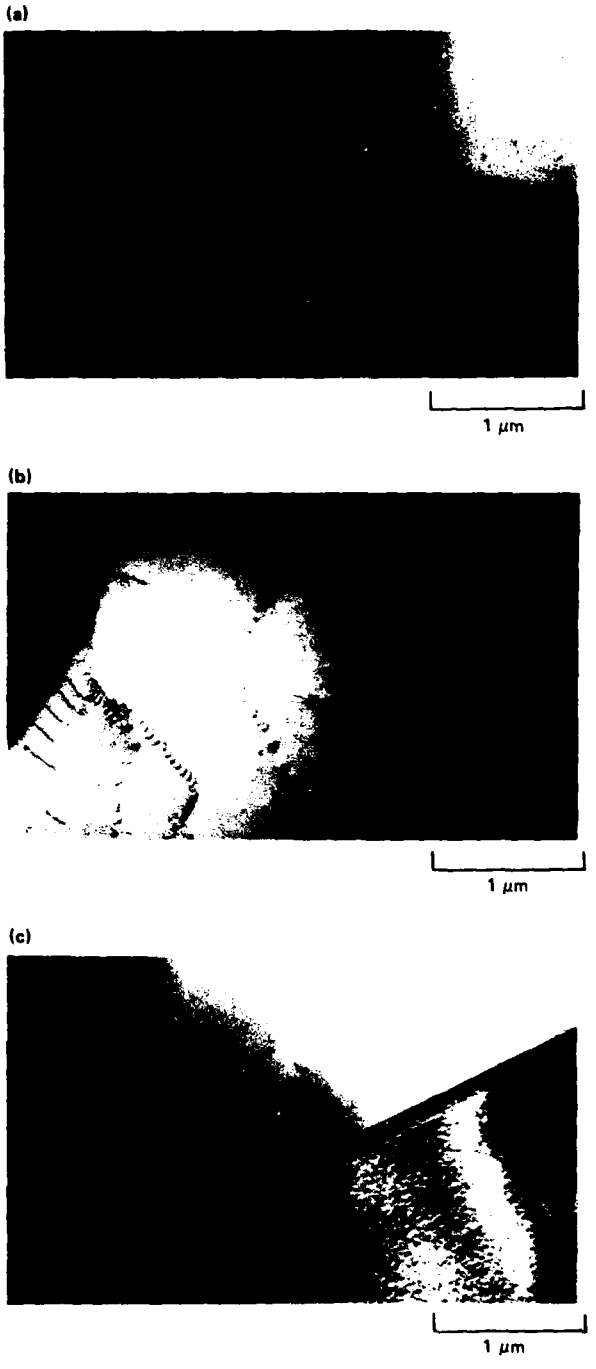

Figure 14. Transmission electron micrographs of (a) Ti-8Al, (b) Ti-8Al-0.05Y, and (c) Ti-8Al-0.2Er aged at 675°C for 24 h and air cooled to 25°C.

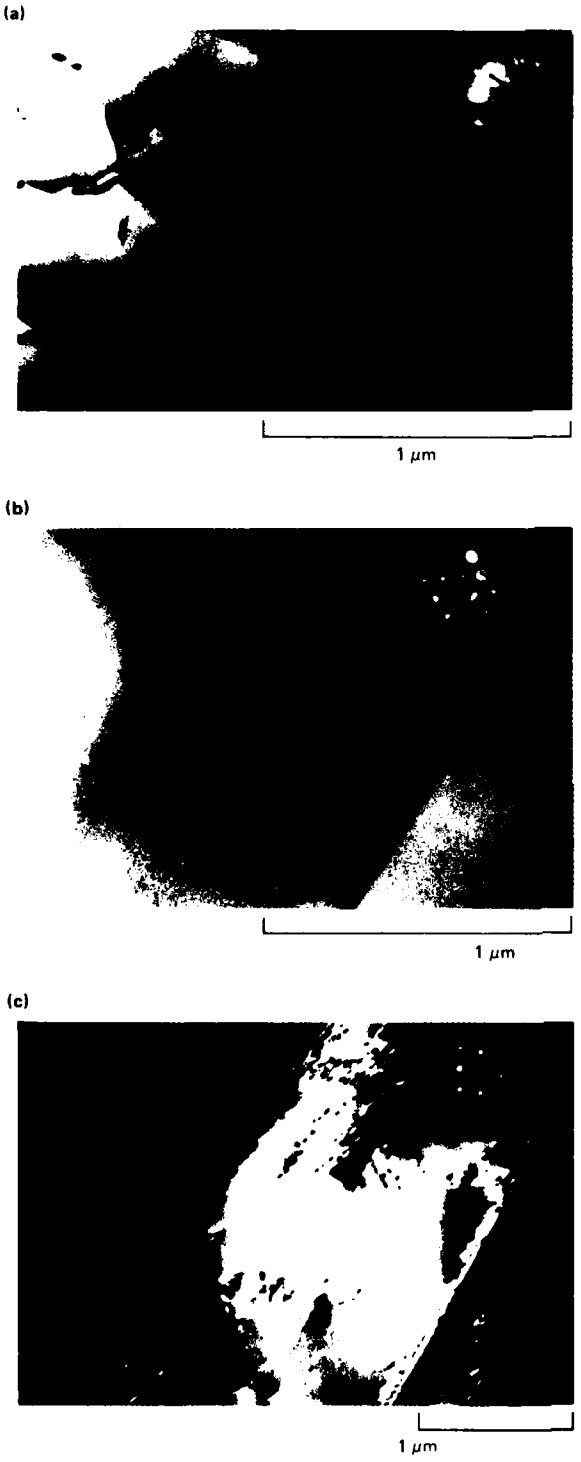

Figure 15. Transmission electron micrographs of (a) Ti-8Al, (b) Ti-8Al-0.1Y, and (c) Ti-8Al-0.2Er aged at 750°C for 21 h and air cooled to 25°C.

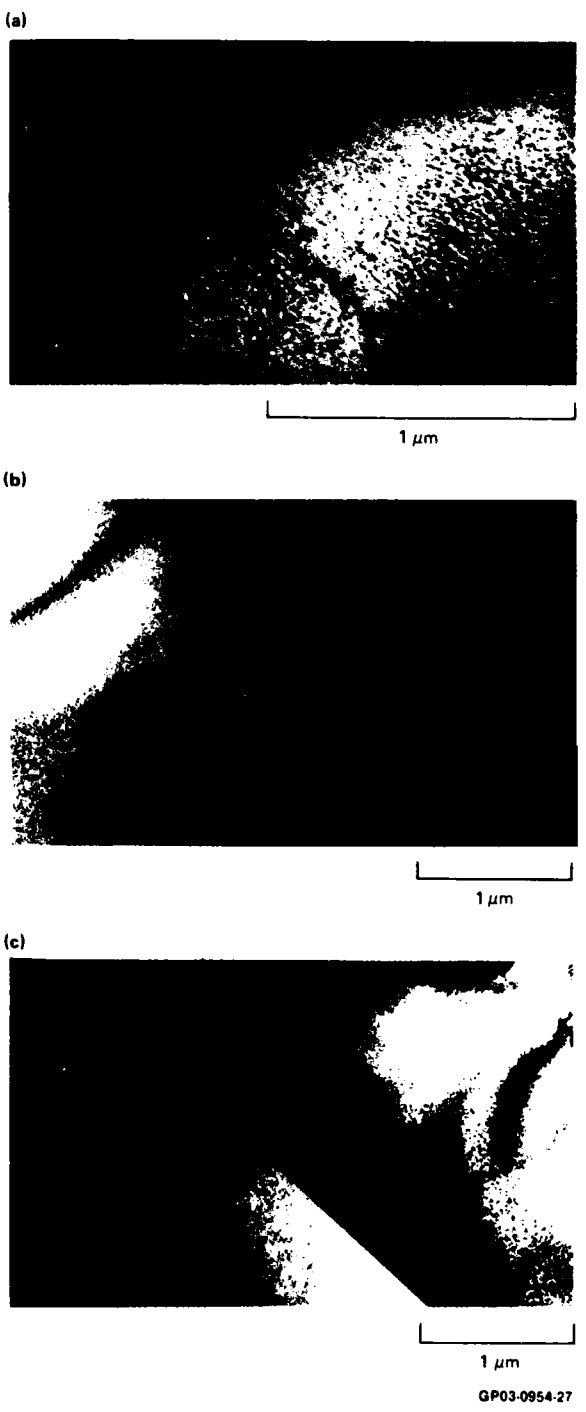

Figure 16. Transmission electron micrographs of (a) Ti-10Al, (b) Ti-10Al-0.1Er, and (c) Ti-10Al-0.2Er aged at 750°C for 21 h and air cooled to 25°C.

4. TENSILE PROPERTIES OF Ti-8Al-RE AND Ti-10Al-RE ALLOYS

The room-temperature tensile properties of Ti-8Al-RE and Ti-10Al-RE alloys with different combinations of grain size and α_2 precipitate density are listed in Tables 4-7 and shown in Figures 17-21. The effects on 0.2% yield stress of grain size and aging treatments indicate that both the unaged and aged alloys exhibit a Hall-Petch dependence of yield stress on grain size. The yield stress increases with increasing volume fraction of α_2 precipitates, and grain size strengthening ($\Delta\sigma_{g\cdot s}$) and precipitation strengthening ($\Delta\sigma_{\alpha_2}$) are linearly additive. The additive behavior of $\Delta\sigma_{g\cdot s}$ and $\Delta\sigma_{\alpha_2}$ indicates that the deformation is transmitted from grain to grain by a simple Hall-Petch type mechanism in which dislocations pile up against the grain boundaries, and the resultant stress concentrations ahead of these pile-ups nucleate dislocation sources in the vicinity of grain boundaries in the neighboring grains. TEM observations of the shearing of the α_2 precipitates by glide dislocations and the resulting formation of narrow planar slip bands support such a hypothesis.

The results in Table 4 indicate that no significant dispersion strengthening occurs in Y- and Er-containing Ti-8Al alloys. The yield stress in aged Ti-8Al-RE alloys containing α_2 precipitates is governed by some form of superposition of the matrix flow stress, precipitation strengthening from α_2 precipitates, and dispersion strengthening from the rare-earth dispersoids. The matrix flow-stress of single-phase Ti-8Al alloys is ≈ 500 MPa, and the precipitation strengthening contribution for the alloys aged at 600°C for 500 h is ≈ 40 MPa. The dispersion strengthening contribution is given by

$$\tau = \frac{1.13\ Gb}{2\pi L} \ln\left(\frac{x}{r_o}\right), \qquad (1)$$

where G is the shear modulus of the matrix, b is the Burgers vector of the dislocation, L is the interparticle spacing, x is the mean particle size, and r_o is the inner cut-off radius, which is considered equal to 4b. Equation (1) is the geometric mean of the bypassing stresses for edge and screw dislocations, and it includes a statistical factor of 0.85 that relates the

macroscopic flow stress to the local Orowan stress. A value of 0.35 for the Poisson ratio of Ti-8Al alloys was used in deriving equation (1). The mean planar center-to-center spacing between the dispersoids, L_c, was calculated from the number of particles, N, in a unit area of the slip plane using the relation $L_c = (N)^{-1/2}$. The mean planar interparticle spacing, L, is then the difference between L_c and the mean particle size, x.

For L = 2.5 μm and x = 100 nm (typical values observed in the Ti-8Al-RE alloys), the flow-stress increase attributable to the dispersoids in polycrystalline Ti-8Al alloys is ≈ 7-20 MPa. The dispersion strengthening is offset to some extent by the softening of the Ti-8Al matrix caused by the scavenging of the interstitial oxygen by rare-earths and consequent reduction in the interstitial oxygen concentration. Thus, the dispersion strengthening contribution is small compared with matrix-flow-stress and precipitation strengthening.

A striking effect of the Er and Y dispersoids is a dramatic increase in ductility of both single-phase and α_2-precipitate-containing Ti-8Al alloys (Figures 17-21). This increased ductility results from dispersal and homogenization of planar slip by the dispersoids. The inconsistencies observed in the effects of dispersoids on the ductility values (Figures 17-21) are believed to be due to variations in the rare-earth concentration from region to region in a single alloy plate. The absence of rare-earth effects on the ductility of alloys containing high rare-earth concentrations is due to the ineffectiveness of coarse particles in modifying the coarse planar slip.

The temperature dependences of the strength and ductility of Ti-8Al-RE and Ti-10Al-RE alloys at 25°, 350°, 450°, 550°, and 600°C are shown in Table 8. The 0.2% yield stress and ultimate tensile strength decrease with increasing temperature, and the total elongation increases. The high-temperature mechanical properties are not significantly altered by Er and Y additions.

TABLE 4. ROOM-TEMPERATURE TENSILE PROPERTIES OF Ti-8Al-RE ALLOYS.

Heat treatment	Yield stress at 0.2% offset (MPa)				Uniform elongation (%)				Ultimate tensile stress (MPa)				Total elongation (%)			
	Ti-8Al	Ti-8Al-0.05Y	Ti-8Al-0.1Y	Ti-8Al-0.2Er	Ti-8Al	Ti-8Al-0.05Y	Ti-8Al-0.1Y	Ti-8Al-0.2Er	Ti-8Al	Ti-8Al-0.05Y	Ti-8Al-0.1Y	Ti-8Al-0.2Er	Ti-8Al	Ti-8Al-0.05Y	Ti-8Al-0.1Y	Ti-8Al-0.2Er
890°C/10 min; air cool at 25°C 675°C/24 h; air cool to 25°C	887	873	876	862	934	928	909	915	12.7	13.7	13.0	12.5	21.7	26.3	27.0	24.5
890°C/10 min; air cool to 25°C 600°C/500 h; air cool to 25°C	832	928	–	883	946	1008	876	944	–	7.0	–	5.1	0.6	8.9	1.6	6.1
950°C/10 min; air cool to 25°C	805	815	822	798	825	847	850	828	16.0	16.5	15.6	17.3	16.8	31.7	29.8	31.2
950°C/10 min; air cool to 25°C 600°C/500 h; air cool to 25°C	877	883	893	867	889	928	943	894	0.5	5.3	9.4	1.2	1.2	6.2	10.3	1.7
980°C/10 min; air cool to 25°C	860	827	844	815	860	860	853	845	13.4	15.2	16.3	16.3	15.2	15.2	28.8	31.4
980°C/10 min; air cool to 25°C 675°C/24 h; air cool to 25°C	814	815	826	814	846	834	856	851	14.4	15.1	14.2	14.9	18.1	24.1	16.2	23.4
980°C/8 h; air cool to 25°C	802	790	788	774	811	821	813	799	1.7	17.8	18.2	18.4	10.1	28.0	30.5	31.2
*980°C/8 h; air cool to 25°C 675°C/24 h; air cool to 25°C	804	806	783	786	817	830	795	819	2.9	17.8	13.2	15.9	7.4	28.8	17.3	23.4
*980°C/8 h; air cool to 25°C 675°C/24 h; air cool to 25°C	771	782	793	764	791	810	811	809	1.7	2.1	8.4	14.6	4.3	3.1	10.3	24.3
980°C/8 h; air cool to 25°C 600°C/500 h; air cool to 25°C	849	841	840	835	861	851	885	852	0.5	0.7	9.4	1.0	1.3	1.2	10.8	1.6

*Duplicate tests

GP03-0854-5

TABLE 5. ROOM-TEMPERATURE TENSILE PROPERTIES OF Ti-8Al ALLOYS WITH HIGH Y AND Er CONCENTRATIONS.

Heat treatment	Orientation	Yield stress at 0.2% offset (MPa)				Ultimate tensile stress (MPa)				Uniform elongation (%)				Total elongation (%)			
		Ti-8Al	Ti-8Al-0.5Y	Ti-8Al-1.0Er	Ti-8Al-2.0Er	Ti-8Al	Ti-8Al-0.5Y	Ti-8Al-1.0Er	Ti-8Al-2.0Er	Ti-8Al	Ti-8Al-0.5Y	Ti-8Al-1.0Er	Ti-8Al-2.0Er	Ti-8Al	Ti-8Al-0.5Y	Ti-8Al-1.0Er	Ti-8Al-2.0Er
950°C/24 h; air cool to 25°C	L	708	741	722	742	761	808	794	829	9.2	8.8	10.5	11.8	12.6	10.7	13.4	14.5
675°C/24 h; air cool to 25°C	T	706	712	741	741	754	753	789	813	2.2	3.0	4.8	8.7	4.5	3.7	5.1	9.0
980°C/2 h; air cool at 25°C	L	699	700	717	720	781	768	800	813	19.3	16.4	16.1	10.4	27.2	19.5	17.4	11.4
980°C/2h; air cool to 25°C 675°C/24 h; air cool to 25°C	T	719	725	740	769	789	789	815	855	10.8	7.5	8.2	10.1	13.5	9.0	8.7	10.7

GP03-0854-6

TABLE 6. ROOM-TEMPERATURE TENSILE PROPERTIES OF Ti-10Al-RE ALLOYS*.

Heat treatment	Ultimate tensile stress (MPa)				Total elongation (%)			
	Ti-10Al	Ti-10Al-0.05Y	Ti-10Al-0.10Y	Ti-10Al-0.2Er	Ti-10Al	Ti-10Al-0.05Y	Ti-10Al-0.1Y	Ti-10Al-0.2Er
980°C/5 min; air cool to 25°C	796	887	882	900	0.7	1.0	0.9	1.4
980°C/5 min; air cool to 25°C 750°C/24 h; air cool to 25°C	801	919	876	757	0.7	0.8	0.6	0.5
980°C/5 min; air cool to 25°C 600°C/500 h; air cool to 25°C	927	827	731	731	0.5	0.5	0.3	0.5
1000°C/4 h; air cool to 25°C	716	798	770	730	0.5	0.7	0.5	0.5
1000°C/4 h; air cool to 25°C 600°C/500 h; air cool to 25°C	597	693	563	610	0.5	0.5	0.4	0.4

* The 0.2% offset yield stress and uniform elongation are not reported because all specimens fractured without significant plastic deformation.

GP03-0954-7

TABLE 7. ROOM-TEMPERATURE TENSILE PROPERTIES OF HOT-ROLLED Ti-10Al WITH HIGH Y AND Er CONCENTRATIONS.

Alloy	Yield stress at 0.2% offset (MPa)	Ultimate tensile stress (MPa)	Uniform elongation (%)	Total elongation (%)
Ti-10Al	741	849	2.7	3.9
Ti-10Al-0.5Y	689	838	2.2	2.4
Ti-10Al-1.0Er	669	809	1.4	1.7

GP03-0954-8

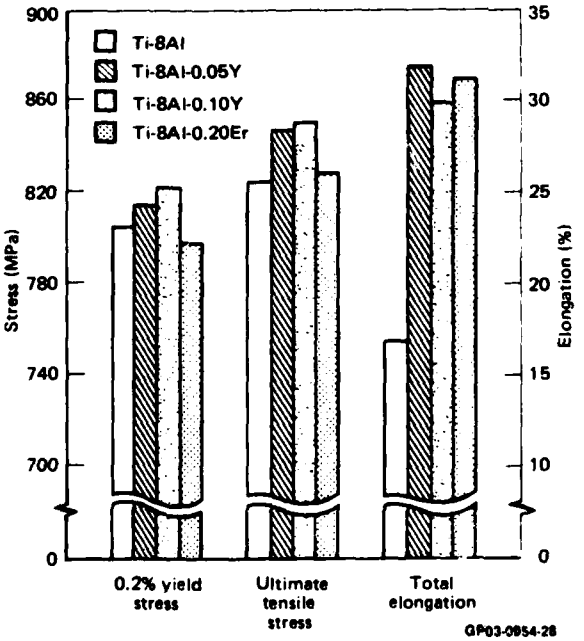

Figure 17. Room-temperature tensile properties of Ti-8Al rare-earth alloys annealed at 950°C for 10 min and air cooled.

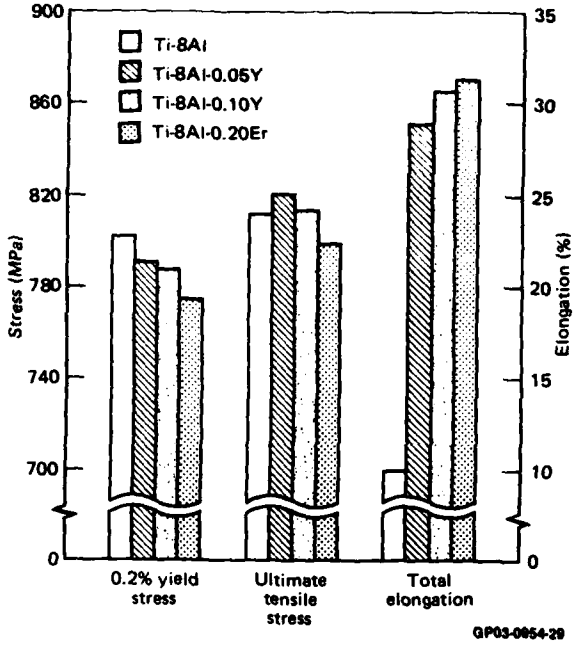

Figure 18. Room-temperature tensile properties of Ti-8Al/rare-earth alloys annealed at 980°C for 8 h and air cooled.

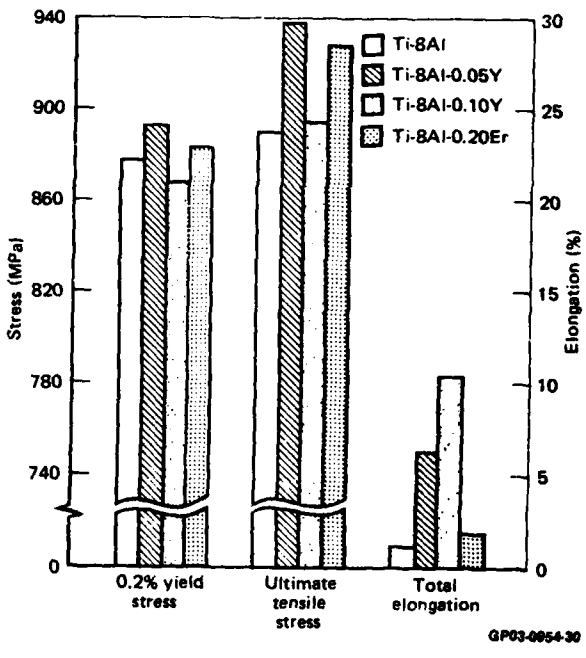

Figure 19. Room-temperature tensile properties of Ti-8Al/rare-earth alloys annealed at 950°C for 10 min and aged at 600°C for 500 h.

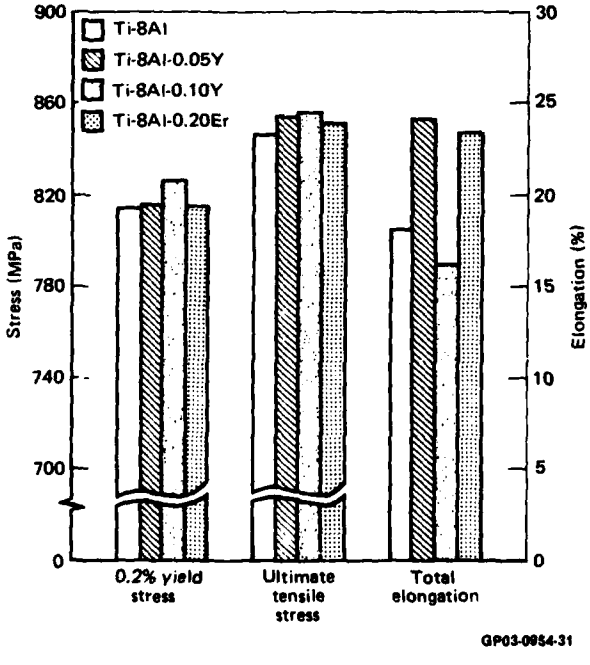

Figure 20. Room-temperature tensile properties of Ti-8Al/rare-earth alloys annealed at 980°C for 10 min and aged at 675°C for 24 h.

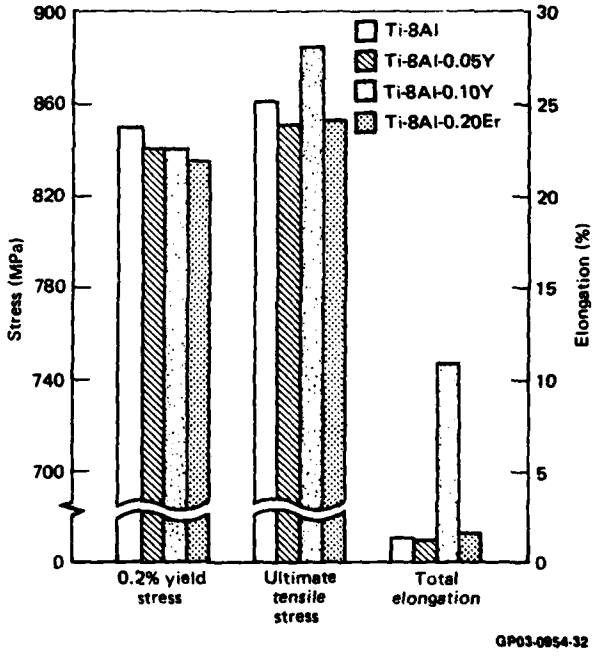

Figure 21. Room-temperature tensile properties of Ti-8Al/rare-earth alloys annealed at 980°C for 8 h and aged at 600°C for 500 h.

TABLE 8. ELEVATED-TEMPERATURE TENSILE PROPERTIES OF Ti-8Al-RE AND Ti-10Al-RE ALLOYS.

Heat treatment	Alloy composition	Yield stress at 0.2% offset (MPa)					Ultimate tensile stress (MPa)					Total elongation (%)				
		25°C	350°C	450°C	550°C	600°C	25°C	350°C	450°C	550°C	600°C	25°C	350°C	450°C	550°C	600°C
950°C/10 min; air cool to 25°C	Ti-8Al	806	–	441	375	–	826	–	547	498	–	16.8	–	35.6	33.5	–
	Ti-8Al-0.05Y	816	426	390	372	349	848	545	496	464	402	31.7	35.0	37.2	47.6	58.6
	Ti-8Al-0.10Y	822	429	394	343	344	851	552	505	455	415	29.8	33.0	35.0	46.5	59.0
	Ti-8Al-0.20Er	798	408	386	356	339	828	545	492	454	377	31.2	33.2	35.8	34.5	58.3
950°C/10 min, air cool to 25°C 675°C/24 h; air cool to 25°C	Ti-8Al	887	–	515	413	–	935	–	605	504	–	21.7	–	25.8	36.8	–
	Ti-8Al-0.05Y	874	520	496	346	324	929	610	586	468	377	26.3	29.6	29.2	43.9	78.5
	Ti-8Al-0.10Y	876	451	388	345	365	909	549	492	442	416	27.0	31.7	34.6	39.2	70.1
	Ti-8Al-0.20Er	862	476	455	553	368	916	572	547	642	418	24.5	26.2	29.3	24.4	49.5
980°C/10 min; air cool to 25°C	Ti-10Al	–	–	–	462	–	796	–	605	556	–	0.7	–	–	23.3	–
	Ti-10Al-0.05Y	–	497	–	476	377	887	626	567	587	460	1.0	30.9	36.9	33.3	51.9
	Ti-10Al-0.10Y	–	490	–	476	395	882	627	–	584	503	0.9	38.5	–	32.6	59.9
	Ti-10Al-0.20Er	–	481	473	475	407	900	624	584	587	505	1.4	36.1	38.1	33.0	34.3
980°C/10 min; air cool to 25°C 675°C/24 h; air cool to 25°C	Ti-10Al	–	–	630	363	–	802	–	716	467	–	0.7	–	26.0	38.9	–
	Ti-10Al-0.05Y	–	689	625	471	439	920	780	718	600	528	0.8	23.2	27.8	32.5	42.9
	Ti-10Al-0.10Y	–	678	630	502	428	876	776	727	595	502	0.6	22.0	26.3	35.0	41.2
	Ti-10Al-0.20Er	–	690	638	498	443	758	778	735	623	526	0.5	22.5	26.5	24.5	26.5

GP03-0954-9

5. FRACTURE MORPHOLOGIES AND DEFORMATION SUBSTRUCTURES OF Ti-8Al-RE AND Ti-10Al-RE ALLOYS

The fracture surfaces of Ti-8Al-RE alloys deformed at 25°C after annealing at 980°C for 8 h and air-cooling to 25°C consist of dimples formed by nucleation, growth, and coalescence of microvoids (Figure 22). In Ti-8Al-RE alloys, fracture initiates at particle-matrix interfaces, resulting in a higher microvoid density and smaller dimple size than in Ti-8Al without rare-earths (Figure 22b).

The Ti-8Al alloys without rare earths but containing α_2 precipitates fracture by cleavage as evidenced by transgranular facets on the fracture surfaces (Figure 23a). The inhomogeneous, coarse slip caused by the shearing of α_2 precipitates by glide dislocations promotes cleavage fracture. In the rare-earth-containing alloys, however, the dispersoids disperse the planar slip, reduce the inhomogeneity of slip, and promote microvoid nucleation; thus fracture occurs by mixed dimple fracture and cleavage in the Ti-8Al-RE alloys (Figure 23b). The observation of dimple fracture in Y- and Er-containing Ti-8Al is consistent with the higher ductility of these alloys. The fracture surfaces of alloys aged at 675°C for 24 h have mixed dimple and cleavage fracture because of a lower volume-fraction of α_2 precipitates (Figure 23). The Ti-10Al-RE alloys exhibit predominantly cleavage fracture (Figure 24).

The deformation substructures in differently heat-treated Ti-8Al-RE alloys are shown in Figures 25-28. Figure 25a shows the slip character of Ti-8Al containing α_2 precipitates produced by aging the alloy at 600°C. The dislocation density is low, and the dislocations are confined to narrow planar slip bands because of shearing of the coherent α_2 particle by glide dislocations. The slip bands are devoid of α_2 particles, indicating that these particles are destroyed in the slip bands by successive movements of the dislocations. In the Y- and Er-containing alloys, the substructure consists of a high density of relatively homogeneously distributed dislocations (Figures 25 and 26), indicating profuse cross slip in these alloys. The tendency for planar slip is significantly reduced by the rare-earth dispersoids, and stress build-up in slip bands is relieved (as shown at S in Figure 26b).

As seen from Figures 25-28, the dispersoids homogenize the slip and refine the substructure formed during deformation. The dispersed phase modifies the slip behavior by providing dislocation sources and barriers to dislocation motion. Dislocations can overcome the dispersed-phase particles by the Orowan bypass and Hirsch cross-slip mechanisms, which result in greater densities of localized channels of dislocations during the initial stages of

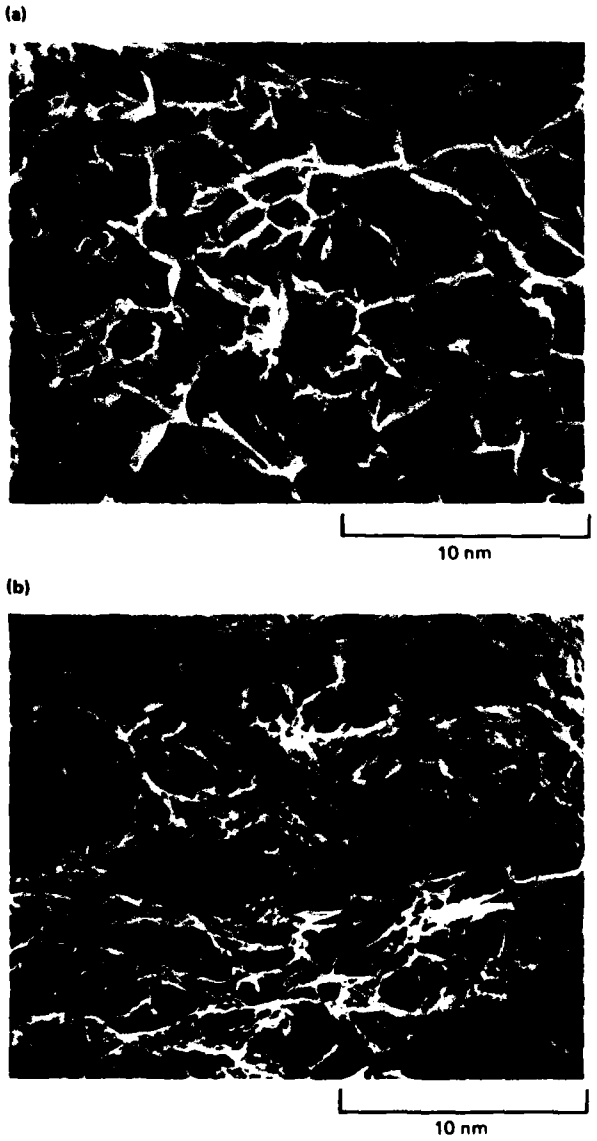

Figure 22. Fractographs of (a) Ti-8Al and (b) Ti-8Al-0.1Y alloys tested in tension at 25°C after annealing at 980°C for 8 h and air cooling to 25°C.

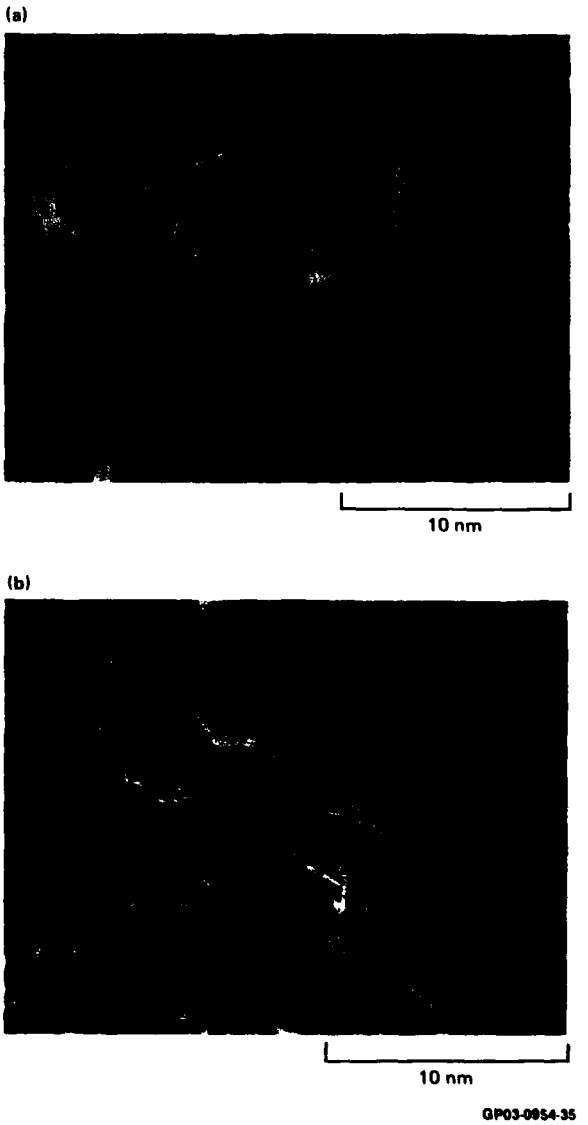

Figure 23. Fractographs of (a) Ti-8Al and (b) Ti-8Al-0.1Y alloys tested in tension at 25°C after annealing at 980°C for 8 h, air cooling to 25°C, aging at 675°C for 24 h, and air cooling to 25°C.

deformation in the presence of dispersoids. As the deformation increases, dislocations are swept into the channels, and well-defined cells are thus formed whose spacing is determined by the spacing of the initial localized channels. At higher temperatures, a decreased planarity of slip accompanied by recovery results in larger dislocation cells.

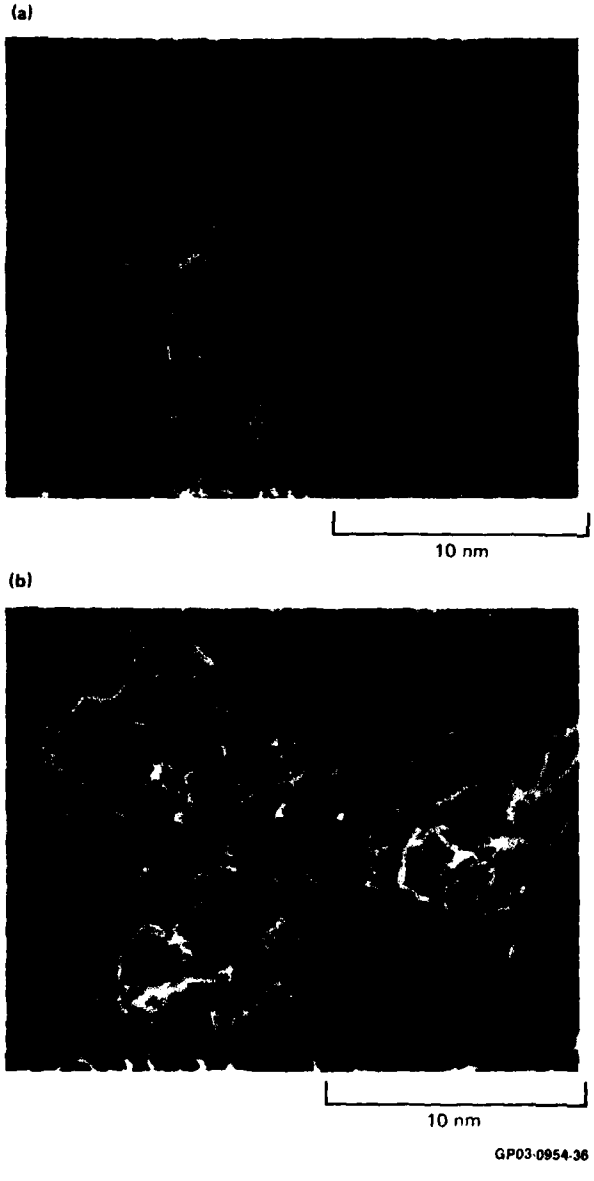

Figure 24. Fractographs of (a) Ti-10Al and (b) Ti-10Al-0.1Y alloys tested in tension at 25°C after annealing at 980°C for 5 min, air cooling to 25°C, aging at 600°C for 500 h, and air cooling to 25°C.

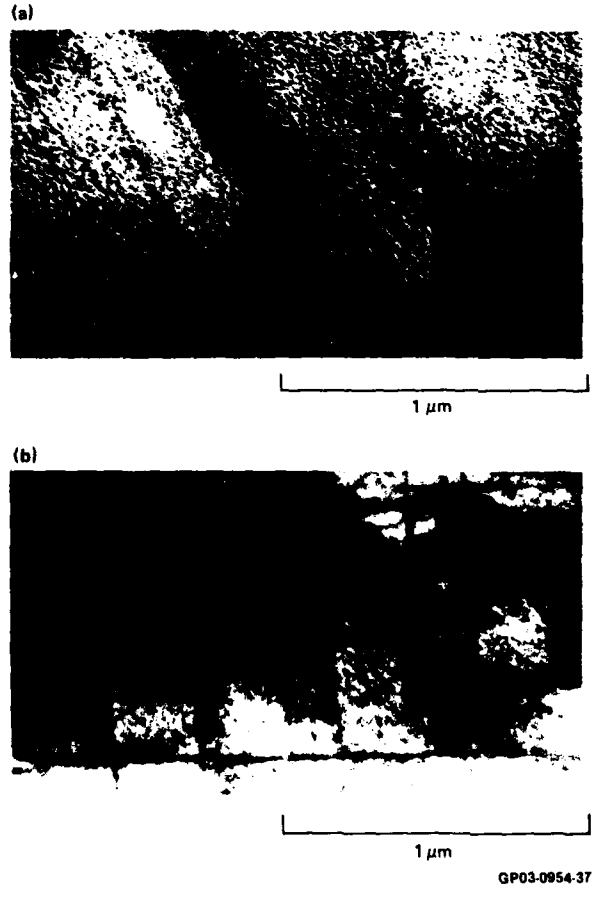

Figure 25. *Dislocation substructures* in (a) Ti-8Al (grain size = 32 μm) and (b) Ti-8Al-0.1Y (grain size = 19 μm) alloys deformed in tension at 25°C after annealing at 950°C for 10 min, air cooling to 25°C, aging at 600°C for 500 h, and air cooling to 25°C.

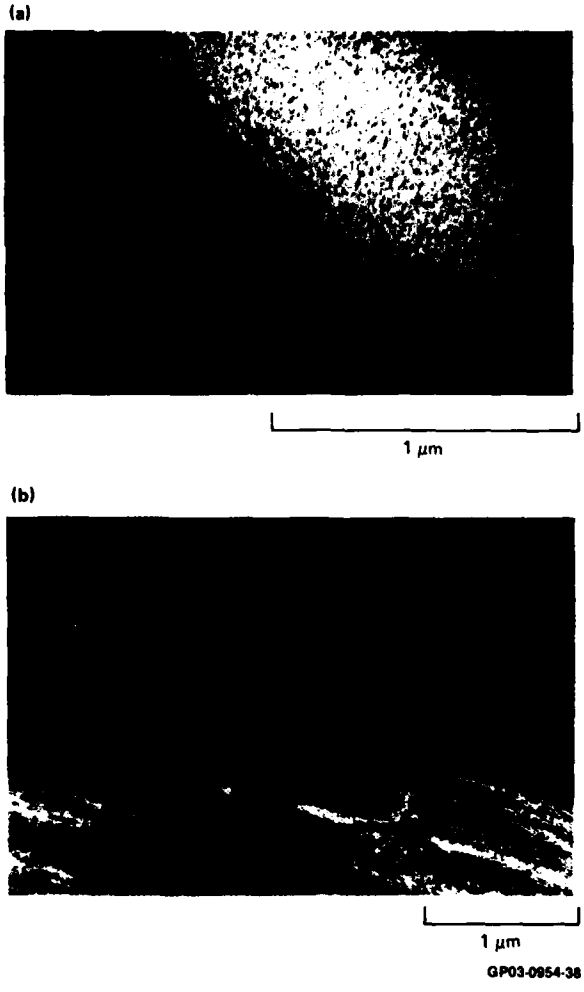

Figure 26. Dislocation substructures in (a) Ti-8Al (grain size = 44 μm and (b) Ti-8Al-0.1Y (grain size = 28 μm) alloys deformed in tension at 25°C after annealing at 900°C for 8 h, air cooling to 25°C, aging at 600°C for 500 h, and air cooling to 25°C.

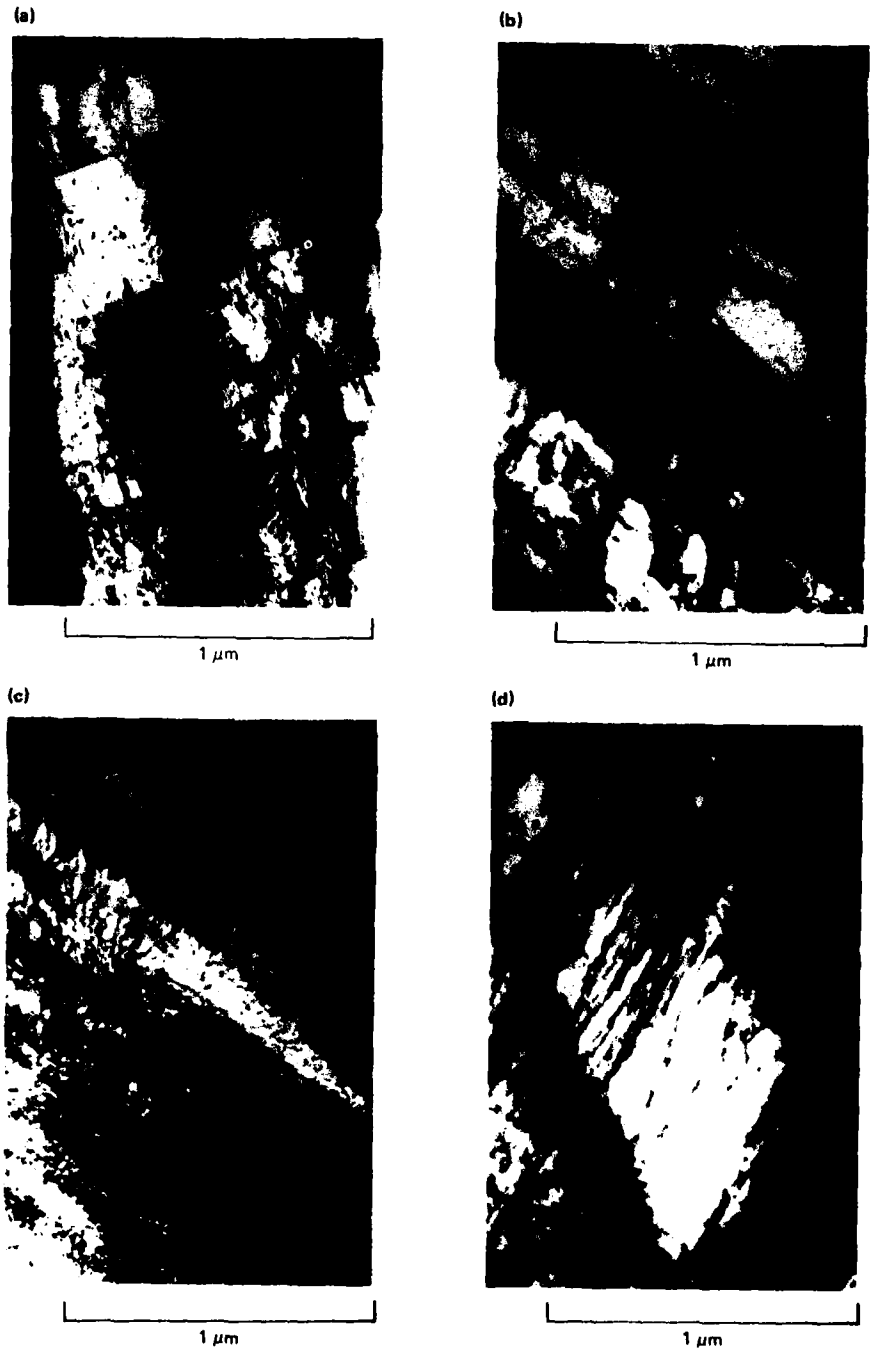

Figure 27. Dislocation substructures in (a) Ti-8Al (grain size = 41 μm), and (b), (c), and (d) Ti-8Al-0.2Er (grain size = 26 μm) deformed in tension at 25°C after annealing at 980°C for 10 min, air cooling at 25°C, aging at 675°C for 24 h, and air cooling to 25°C.

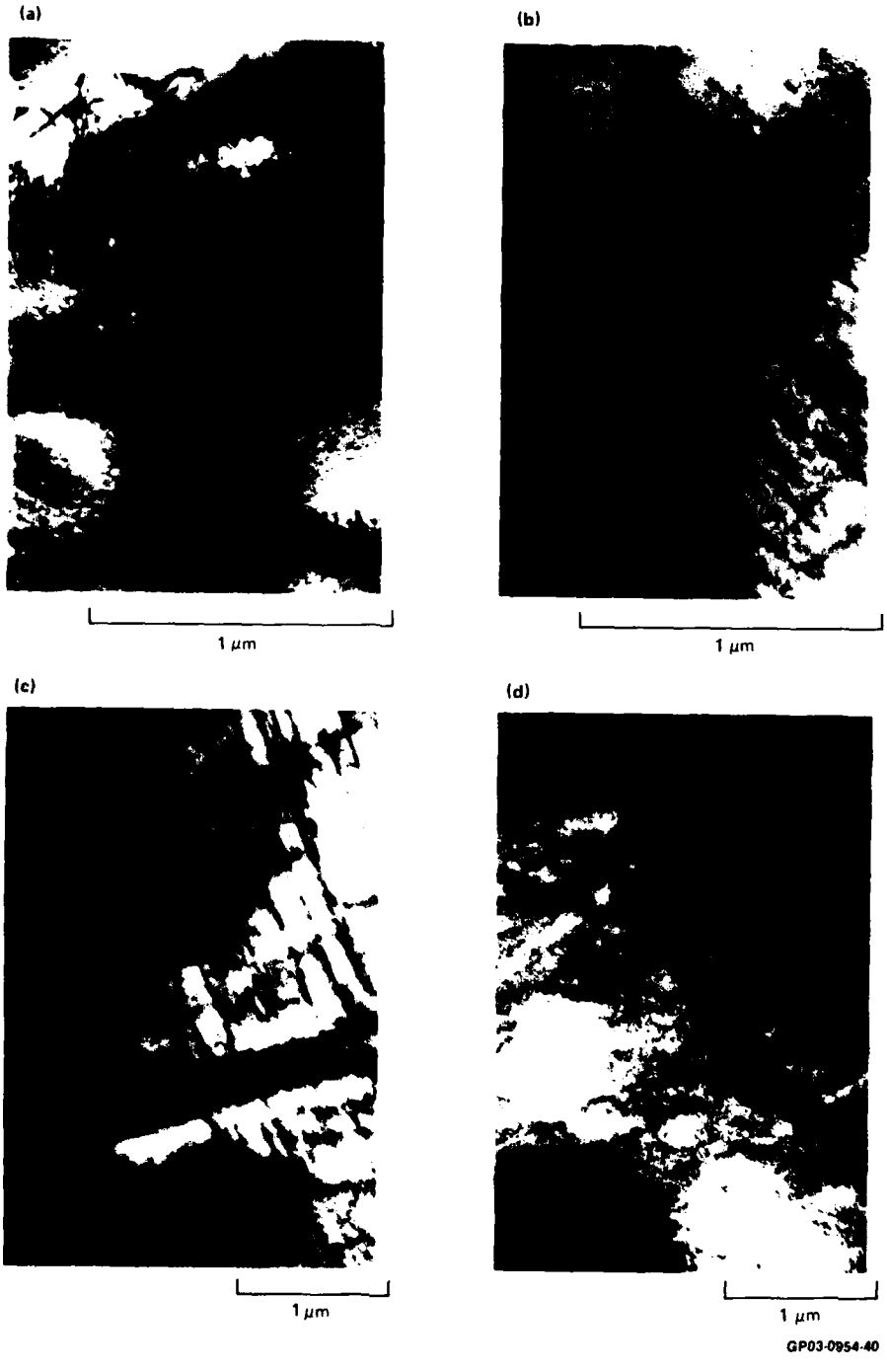

Figure 28. Dislocation substructures in (a, b) Ti-8Al (grain size = 41 μm) and (c, d) Ti-8Al-0.1Y (grain size = 25 μm) deformed in tension at 25°C after annealing at 980°C for 10 min, air cooling to 25°C, aging at 675°C for 24 h, and air cooling to 25°C.

6. CREEP DEFORMATION OF Ti-8Al-RE AND Ti-10Al-RE ALLOYS

The steady-state creep rates, stress exponents, and apparent activation energies for creep of single-phase and α_2-precipitation-strengthened Ti-8Al and Ti-10Al alloys were determined at 400-650°C. An increasing Al concentration and increasing volume-fraction of α_2 precipitates decrease the creep rates as shown in Figures 29 and 30. The stress dependence of the steady-state creep rate of single-phase Ti-8Al and Ti-10Al alloys follows power laws with exponents ≈ 3 at low stress and ≈ 9 at high stresses. The presence of α_2 precipitates results in a lowering of the stress exponent at low stresses. The steady-state creep rates at 600°C are significantly lower for the Ti-8Al and Ti-10Al alloys than for Ti-6Al-4V (Figure 31).

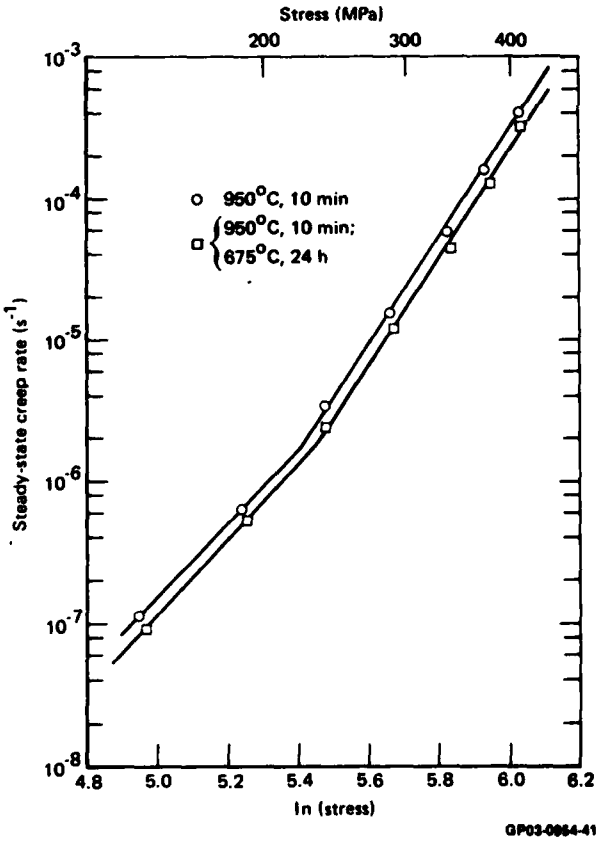

Figure 29. Effect of annealing on the stress dependence of steady-state creep rate at 600°C in Ti-8Al.

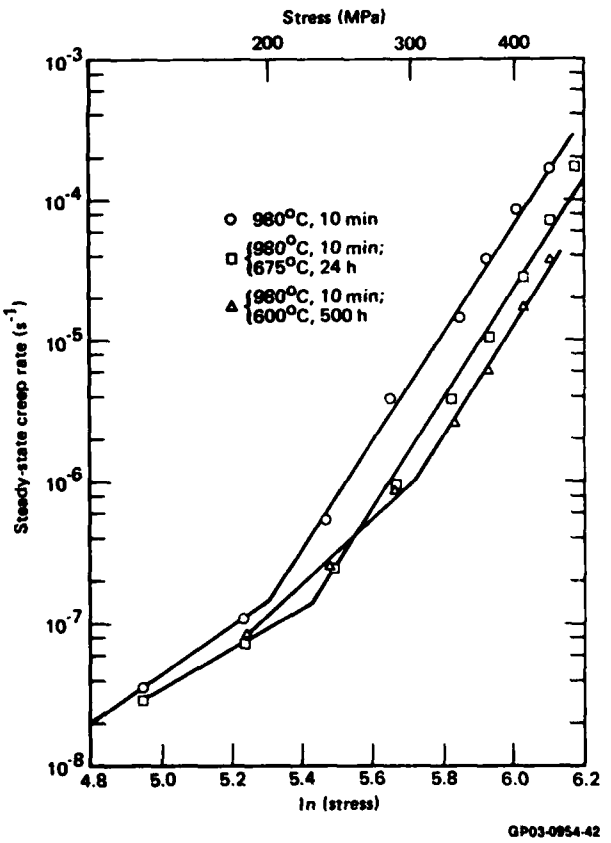

Figure 30. Effect of annealing on the stress dependence of steady-state creep rate at 600°C in Ti-10Al.

Yttrium does not alter the creep rates in precipitation-annealed Ti-8Al and Ti-10Al, but in the alloys annealed in the single-phase α region, Y increases the creep rate. The activation energy for creep of single-phase alloys, ΔH_{α}, is greater than that of α_2-precipitation-annealed alloys, $\Delta H_{\alpha 2}$ (Figures 32 and 33), with both ΔH_{α} and $\Delta H_{\alpha 2}$ being significantly higher than the activation energy for self diffusion of titanium. The activation energies for creep of differently heat-treated alloys are listed in Table 9.

The deformation substructure formed by creep at 650°C in aged Ti-8Al-0.1Y, shown in Figures 34-37, consists of a high density of tangled and relatively homogeneously distributed dislocations; this substructure is typical of Ti-Al alloys deformed at high temperatures. The activation energy for cross slip is reduced, cross slip is easily activated, and deformation is more homogeneous at high temperatures.

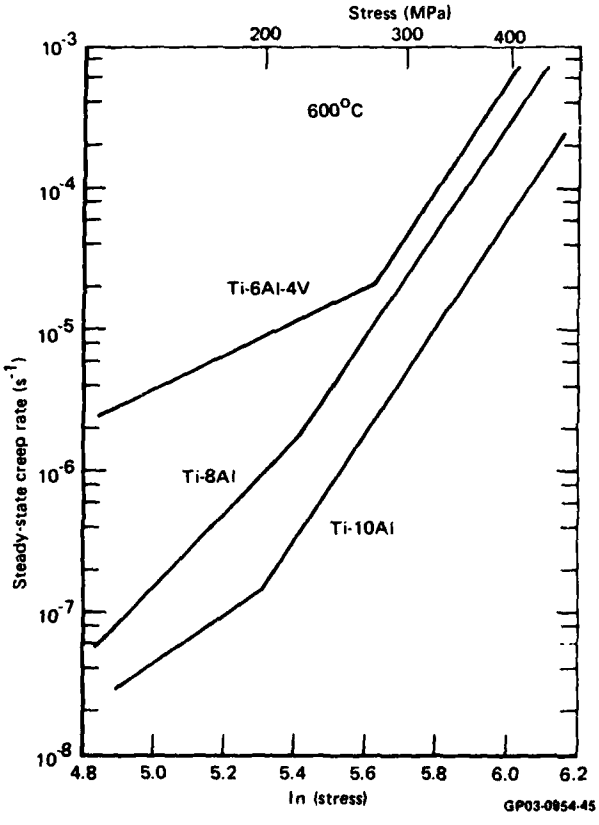

Figure 31. Comparison of creep rates of Ti-8Al, Ti-10Al, and Ti-6Al-4V.

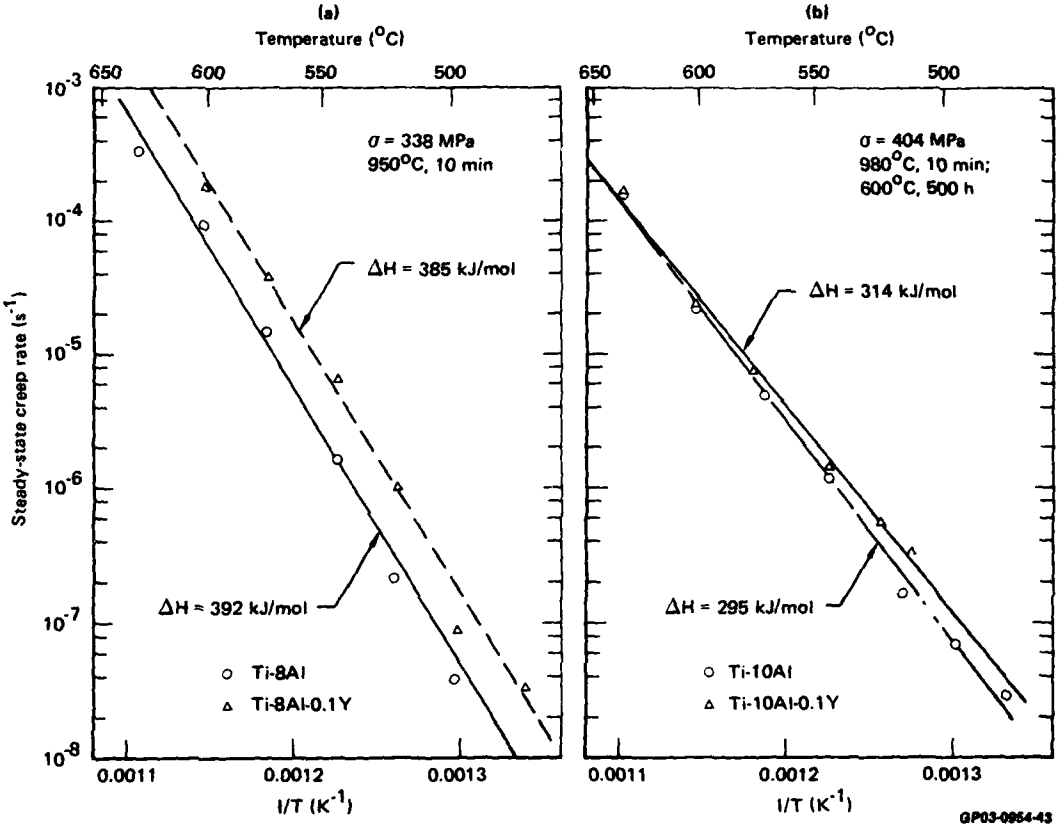

Figure 32. Effect of rare-earth addition on the temperature dependence of steady-state creep rate in (a) Ti-8Al and (b) Ti-10Al alloys.

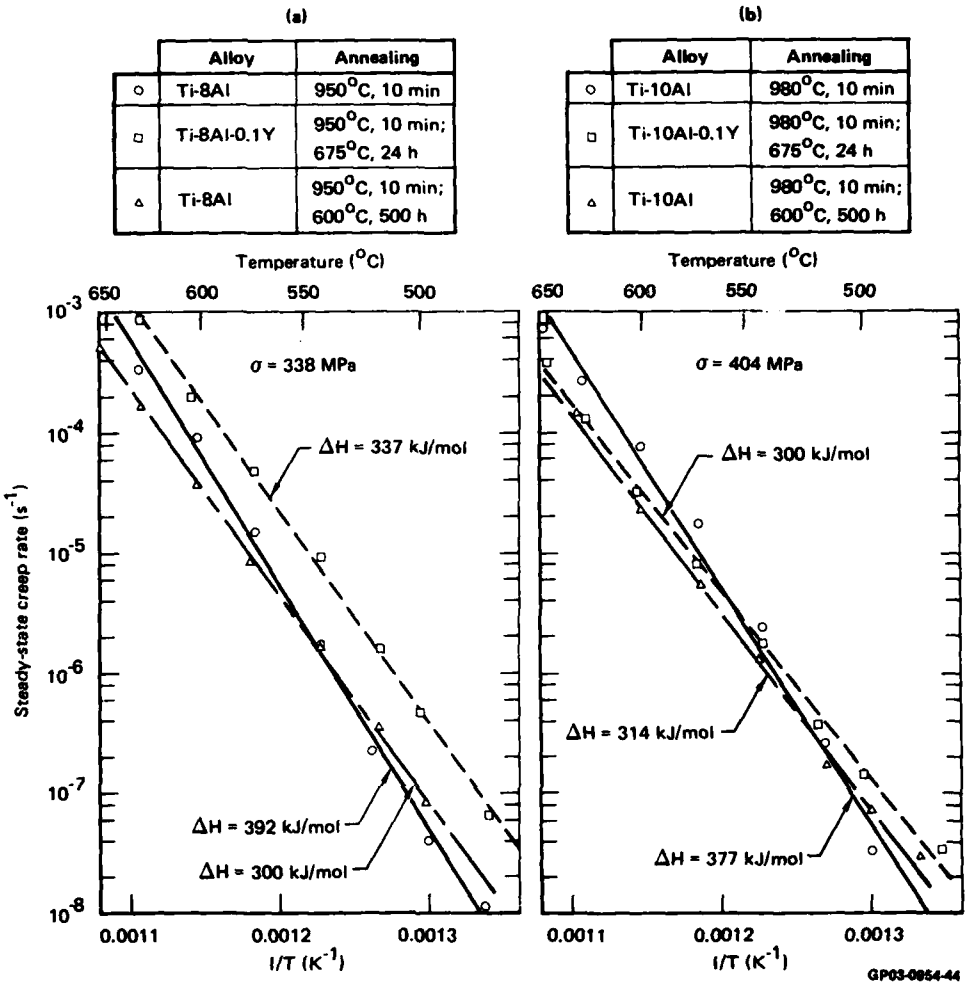

Figure 33. Effect of annealing on the temperature dependence of steady-state creep rate in (a) Ti-8Al and (b) Ti-10Al alloys.

TABLE 9. ACTIVATION ENERGIES FOR CREEP OF Ti-8Al-RE AND Ti-10Al-RE ALLOYS.

Heat treatment	Activation energy (kJ · mol^{-1})			
	Ti-8Al	Ti-8Al-0.1Y	Ti-10Al	Ti-10Al-0.1Y
980°C/10 min; air cool to 25°C	392	385	375	–
980°C/10 min; air cool to 25°C 657°C/24 h; air cool to 25°C	–	337	–	300
980°C/10 min; air cool to 25°C 600°C/500 h; air cool to 25°C	300	–	314	295

GP03-0954-10

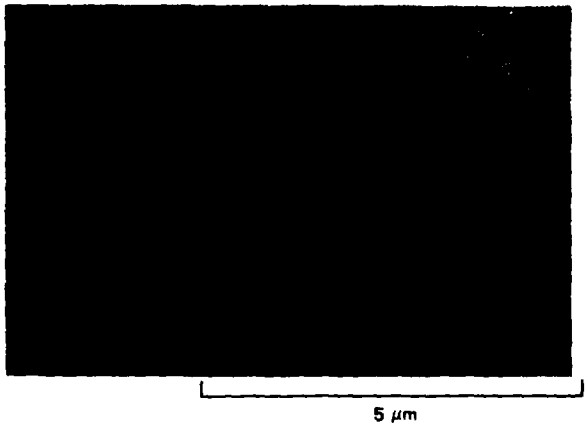

Figure 34. High-magnification transmission electron micrograph of Ti-10Al deformed in creep at a stress of 404 MPa at 475 - 650°C after annealing at 980°C for 10 min, air cooling to 25°C, aging at 600°C for 500 h, and air cooling to 25°C.

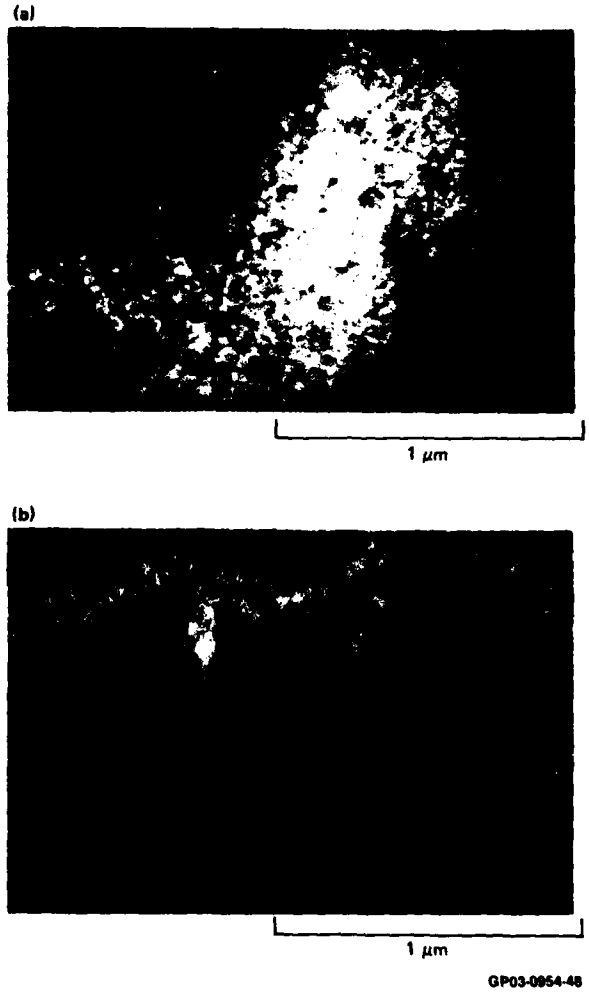

Figure 35. Dislocation substructures in Ti-10Al deformed in creep at a stress of 404 MPa at 475 - 650°C after annealing at 980°C for 10 min, air cooling for 25°C, aging at 600°C for 500 h, and air cooling to 25°C: (a) g = (0002) and (b) g = (0110).

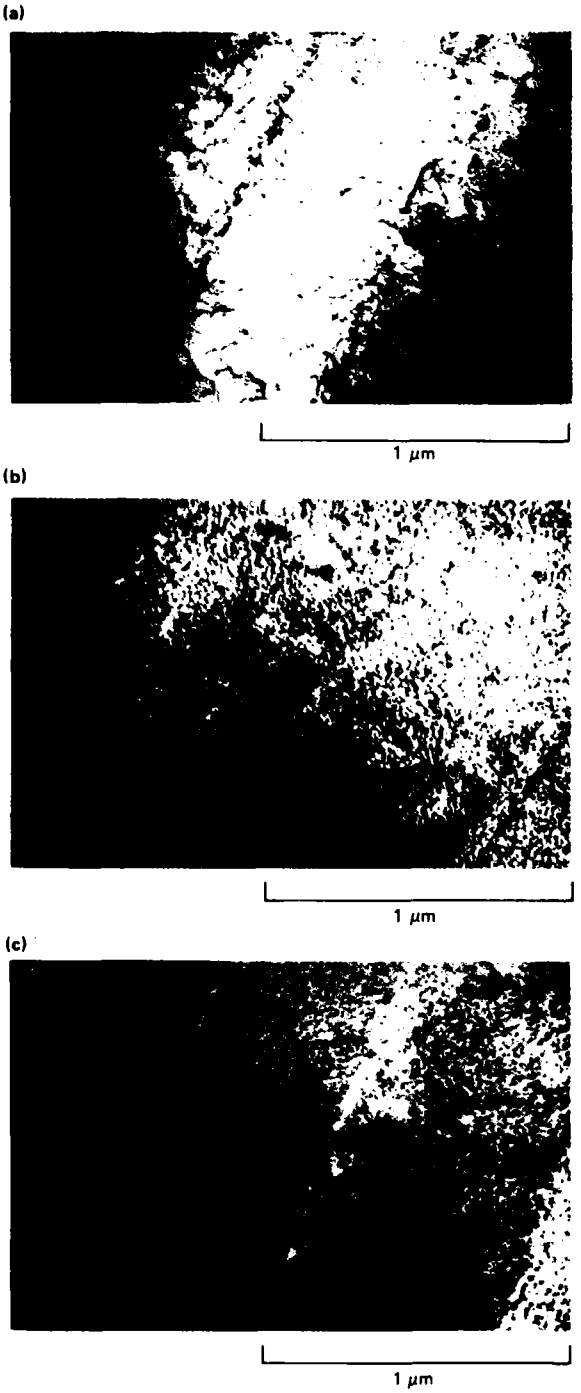

Figure 36. Dislocation substructure in Ti-8Al-0.1Y deformed in creep at a stress of 338 MPa at 475 - 650°C after annealing at 980°C for 10 min, air cooling to 25°C, aging at 675°C for 24 h, and air cooling to 25°C: (a) bright-field micrograph under many-beam condition, (b) dark-field micrograph with matrix reflection $\underline{g} = 0\bar{1}11$, and (c) dark-field micrograph with precipitate reflection.

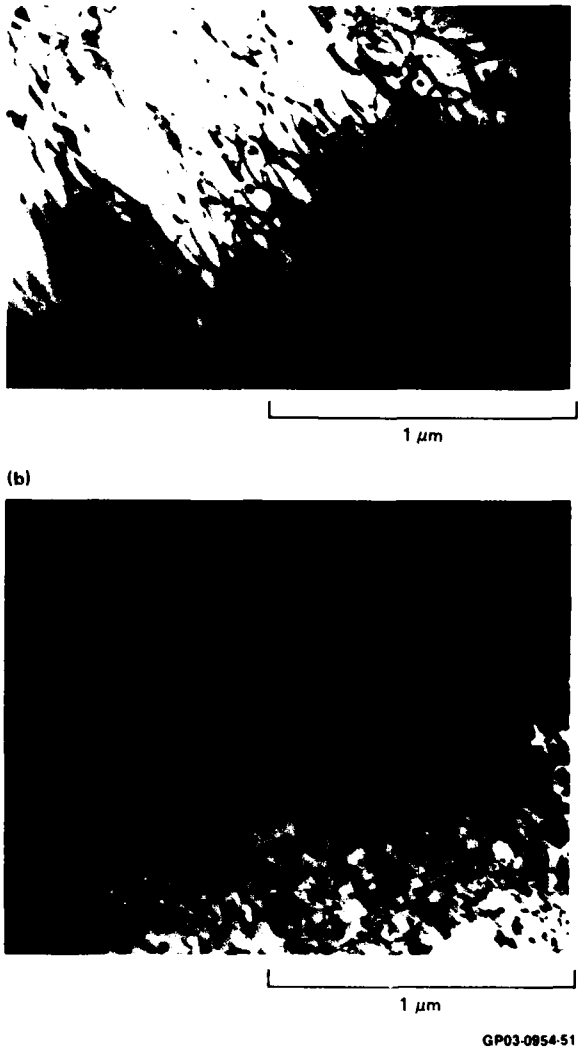

Figure 37. Dislocation substructure in Ti-8Al-0.1Y deformed in creep at a stress of 338 MPa at 475 - 650°C after annealing at 950°C for 10 min and air cooling to 25°C: (a) bright-field micrograph under many-beam conditions and (b) bright-field micrograph with $\underline{g} = (10\bar{1}0)$.

7. LOW-CYCLE FATIGUE OF Ti-8Al-RE AND Ti-10Al-RE

7.1 Low-Cycle Fatigue Characteristics

The low-cycle fatigue characteristics of Ti-8Al-RE and Ti-10Al-RE alloys were measured as functions of microstructure and temperature. Table 10 lists the heat treatment schedules used to obtain single-phase alloys (heat treatment 1), two-phase alloys with fine, coherent, Ti_3Al (α_2) precipitates (heat treatment 2), and two-phase alloys with coarse, semicoherent, Ti_3Al precipitates (heat treatment 3).

The low-cycle fatigue characteristics of the alloys were determined under alternate tension-compression at constant plastic-strain amplitudes of ± 0.125 - 0.5%. The geometry of the low-cycle fatigue specimens is shown in Figure 38.

The specimens and grip assembly were enclosed in a resistance-wound split furnace and equilibrated at the test temperature for 1 h prior to testing. Plastic-strain amplitude was controlled manually for the first few cycles by activating the cycling controls when the desired tension and compression strain limits were reached. The nominal strain rate was maintained at ~1.36×10^{-3} s^{-1} during the first 10 cycles, after which the strain rate was doubled. Figure 39 is a schematic of the hysteresis loop generated during the alternate tension-compression fatigue testing of Ti-8Al alloy at 600°C at a plastic strain amplitude ± 0.5%. After the first few cycles, the cycling was switched to an automatic mode. The automatic control of the constant-plastic-strain amplitude was obtained by activating the cyclic controls of the MTS machine at the points of peak loads along the lines drawn on the chart paper

TABLE 10. HEAT TREATMENTS AND MICROSTRUCTURES OF Ti-8Al-RE AND Ti-10Al-RE ALLOYS SELECTED FOR LOW-CYCLE FATIGUE CHARACTERIZATION.

Heat treatment	Alloy		Microstructure
	Ti-8Al-RE	Ti-10Al-RE	
1	950°C/30 min/AC	980°C/30 min/AC	Single phase
2	600°C/500 h/AC	600°C/500 h/AC	Fine coherent α_2 in Ti-Al matrix
3	950°C/30 min/AC + 650°C/48 h/AC	980°C/30 min/AC +650°C/48 h/AC	Coarse semi-coherent α_2 precipitates in Ti-Al matrix

AC = air cool

GP03-0964-11

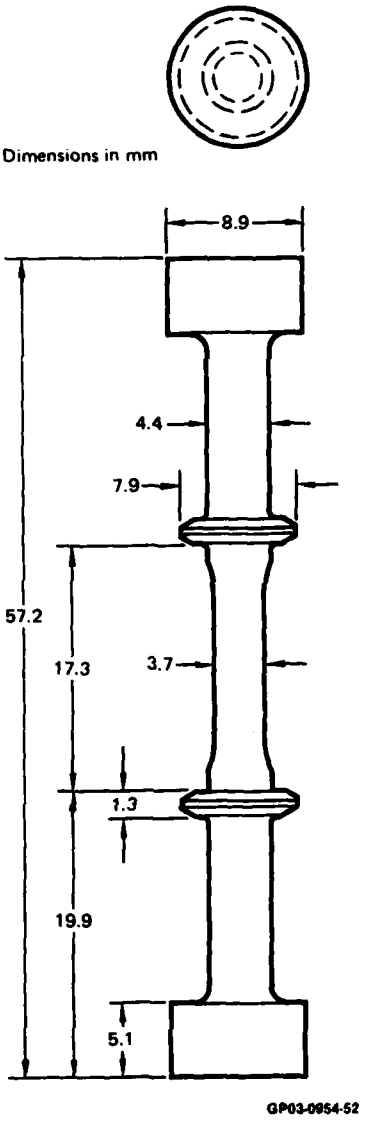

Figure 38. Low-cycle fatigue specimen.

passing through $(+\gamma_{p,\,0})$ and $(-\gamma_{p,\,0})$, where γ_p is the desired strain amplitude, and having slopes corresponding to the elastic modulus of the system. The specimens were tested at several constant-plastic-strain amplitudes in the range 0.125-0.5%, and testing was continued until saturation or final fracture. After the tests, the specimens were immediately fan cooled to room temperature to minimize oxidation of the fracture surfaces and post-fatigue recovery.

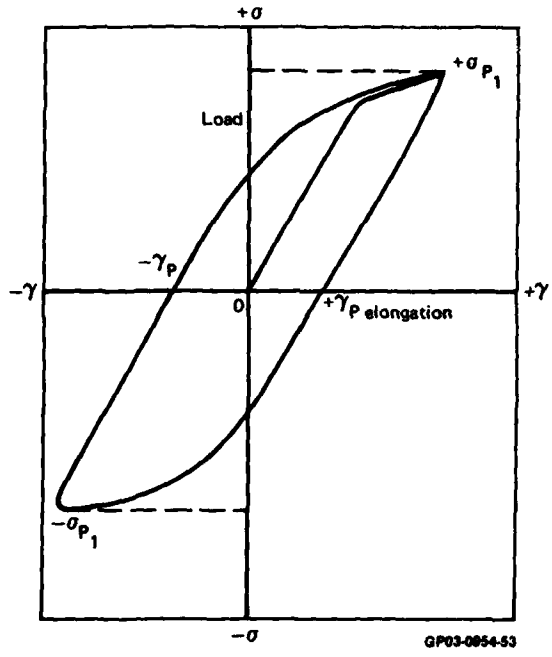

Figure 39. Schematic of the hysteresis loop generated during the alternate tension-compression fatigue testing of Ti-8Al alloy at 600°C at a plastic strain amplitude of ±0.5%.

The low-cycle fatigue behavior of differently heat-treated Ti-8Al-RE and Ti-10Al-RE alloys is shown in Figures 40-42. When the stress axis is parallel to the rolling direction (longitudinal orientation), the Ti-8Al-RE and Ti-10Al-RE alloys have longer fatigue life than the control alloys.

The effects of annealing treatments on the low-cycle fatigue behavior of Ti-10Al and Ti-10Al-0.1Y alloys, shown in Figures 43a and 43b, indicate that the coherent α_2 precipitates increase saturation and fracture stresses and produce fatigue softening. The alloys annealed at 980°C do not exhibit appreciable change in peak stress with increasing number of cycles. The Y dispersoids increase the fatigue life of Ti-10Al without appreciably changing the fatigue-saturation stress.

A striking feature of the effects of temperature upon the low-cycle fatigue behavior of Ti-8Al and Ti-10Al alloys, shown in Figures 44a and 44b, is that even at temperatures as high as 600°C, the alloys have fatigue-saturation stresses in excess of 500 MPa.

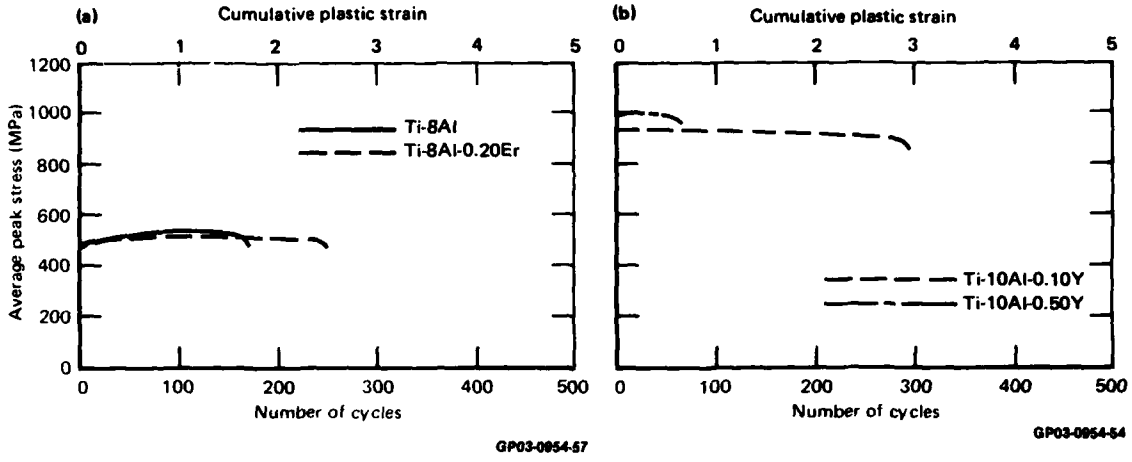

Figure 40. Dependence of peak stress on the number of cycles in the transverse orientation of (a) Ti-8Al-RE alloys deformed in fatigue at 500°C at a plastic strain amplitude of 0.5% and (b) Ti-10Al-RE alloys deformed in fatigue at 25°C at a plastic strain amplitude of ±0.5%.

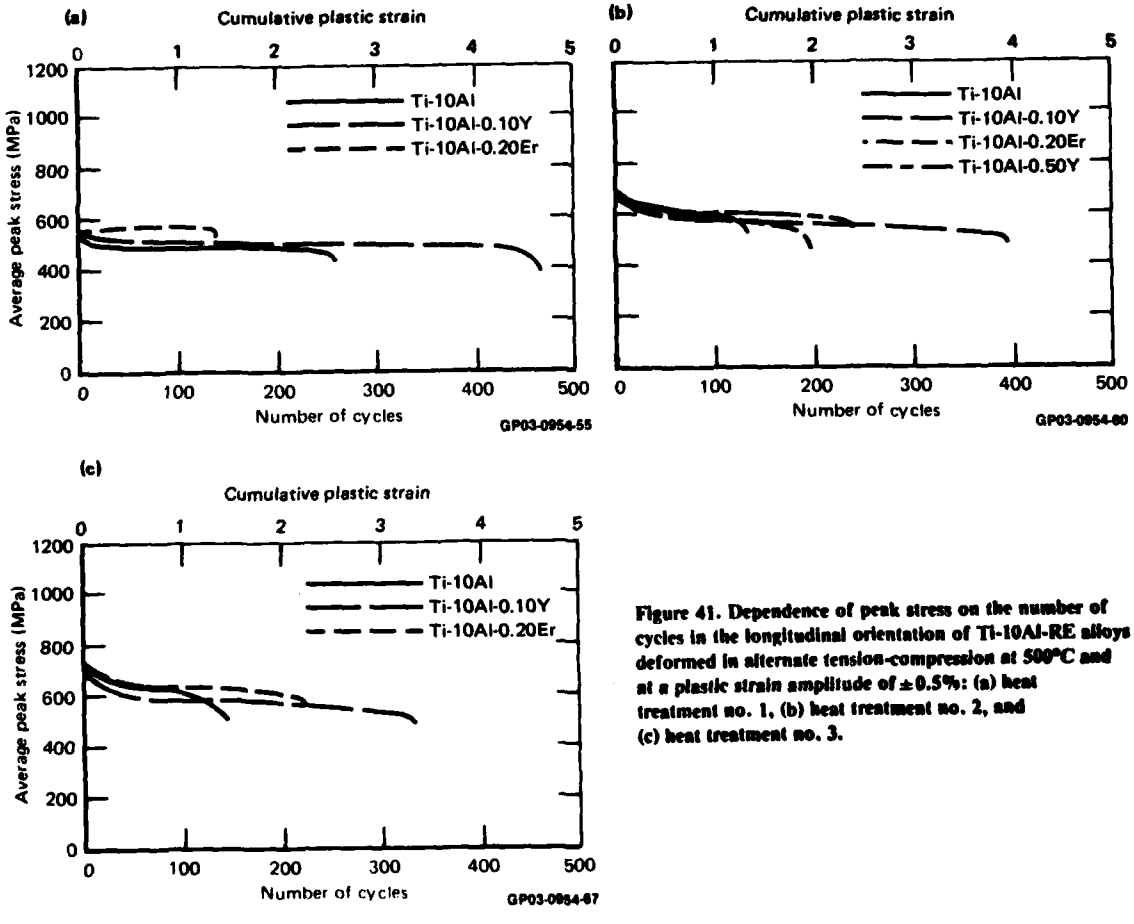

Figure 41. Dependence of peak stress on the number of cycles in the longitudinal orientation of Ti-10Al-RE alloys deformed in alternate tension-compression at 500°C and at a plastic strain amplitude of ±0.5%: (a) heat treatment no. 1, (b) heat treatment no. 2, and (c) heat treatment no. 3.

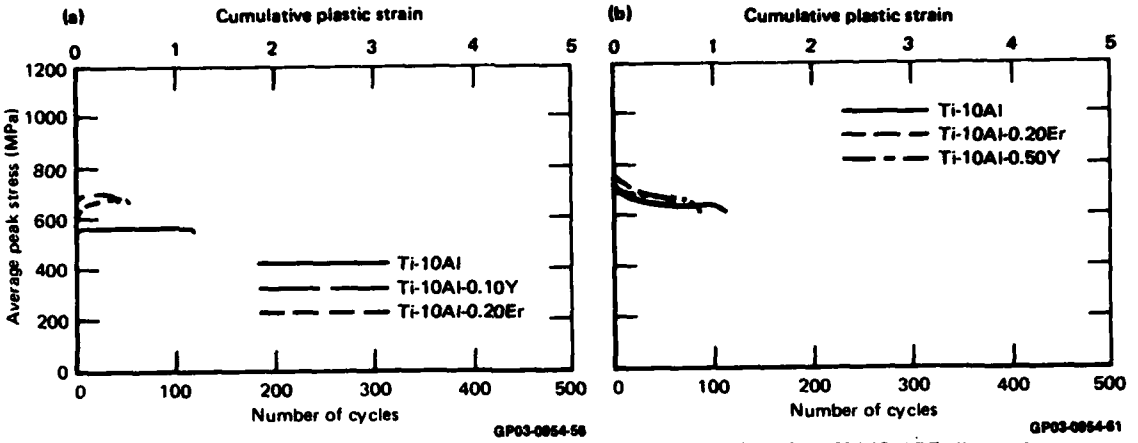

Figure 42. Dependence of peak stress on the number of cycles in the transverse orientation of Ti-10Al-RE alloys deformed in alternate tension-compression fatigue at 500°C at a plastic strain amplitude of ±0.5%: (a) heat treatment no. 1 and (b) heat treatment no. 2.

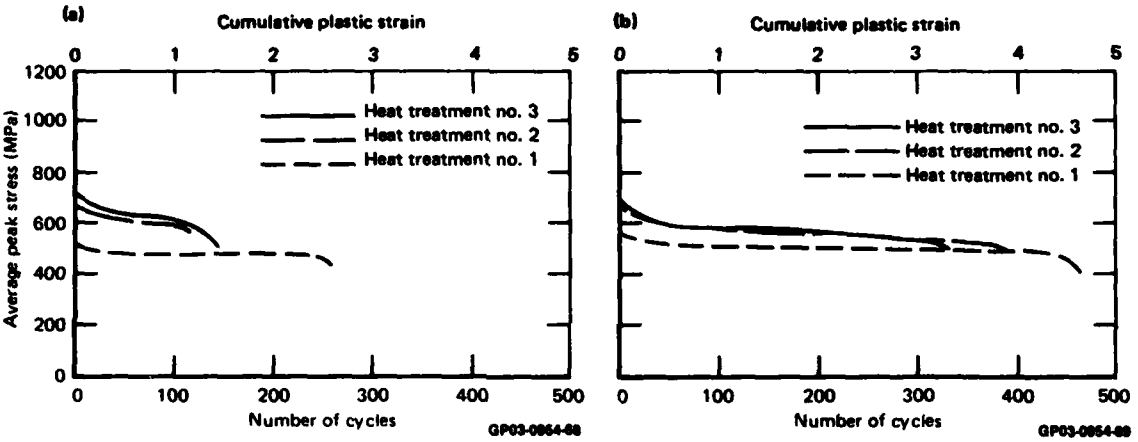

Figure 43. Effect of heat treatment on the low-cycle fatigue behavior of (a) Ti-10Al and (b) Ti-10Al-01.Y deformed in alternate tension-compression fatigue at 500°C at a plastic strain amplitude of ±0.5%.

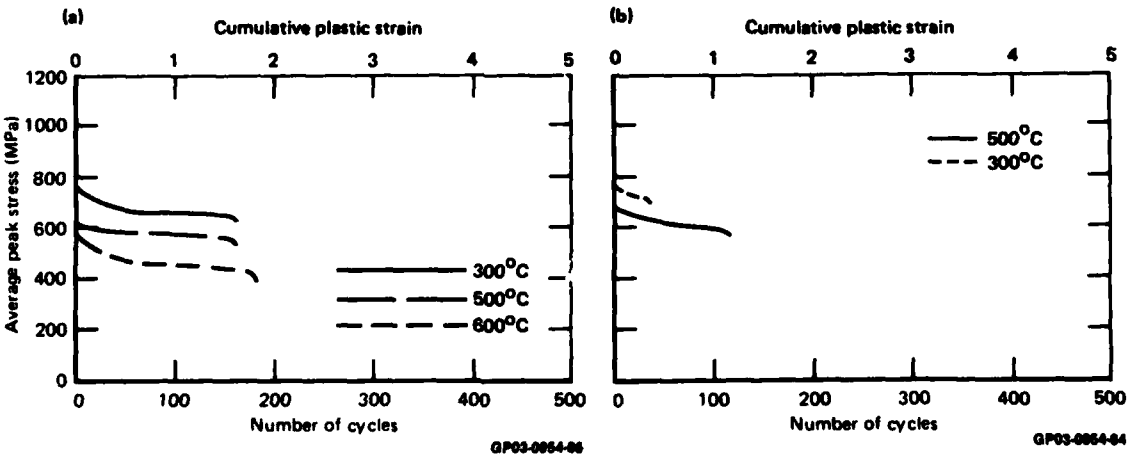

Figure 44. Low-cycle fatigue behavior as a function of temperature in the longitudinal orientation for (a) Ti-8Al (heat treatment no. 3) and (b) Ti-10Al (heat treatment no. 2) deformed in alternate tension-compression at a plastic strain of ±0.5%.

7.2 Fracture Morphologies and Deformation Substructures

The fracture surfaces of Ti-8Al and Ti-8Al-0.1Y specimens failed in fatigue at 500°C are shown in Figures 45 and 46, respectively. The fatigue fracture of Ti-8Al is characterized by extensive transgranular cleavage as indicated by a high density of river patterns, which are characteristic of this type of fracture. Several secondary cracks are distributed in the interior of the grains (as at A in Figure 45), and some intergranular fracture is also indicated. Fatigue striations, which are related to the number of cycles for fatigue crack propagation, are few in number, indicating that crack nucleation is the critical event in controlling the fatigue life in these alloys. The fracture surface of Ti-8Al-0.1Y alloy has a mixed dimple-cleavage appearance (Figure 46), with each dimple containing a dispersoid. The longer fatigue lives observed in Y- and Er-containing alloys thus result from crack propagation by microvoid nucleation and growth.

The deformation substructures in Ti-Al specimens deformed in alternating tension-compression at 25°C and 500°C are shown in Figures 47-52. Ti-8Al specimens deformed at 25°C contain planar bands of dislocations of predominantly $a/3$ $\langle 11\bar{2}0 \rangle$ Burgers vector. High densities of dislocation dipoles, jogged segments, and primatic loops occur between the bands. In the Ti-8Al-0.1Y alloy, two distinct types of dislocation distribution are observed. The regions depleted of rare-earth dispersoids contain planar bands as shown in Figure 48a, and in regions containing the dispersoids, the dislocations are distributed more homogeneously (Figure 48b).

In specimens fatigued at 500°C, the planarity of dislocations is considerably reduced because of increased thermally activated cross-slip and climb. The tendency for planar slip is more pronounced in specimens containing α_2 precipitates, and planar slip bands formed by the shearing of α_2 precipitates are observed at temperatures as high as 500°C. The shearing of α_2 precipitates also results in a continuous dissolution of the precipitates and consequently a decrease in flow stress with increasing number of cycles.

(a)

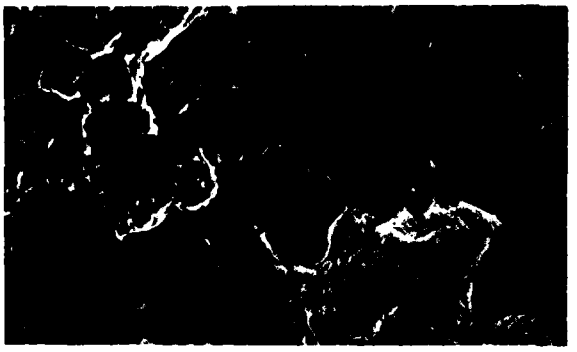

(b)

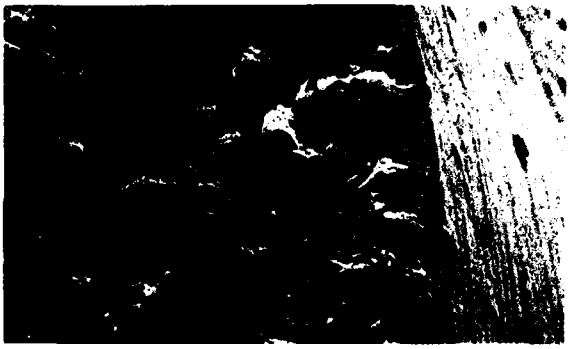

(c)

GP03-0954-70

Figure 45. Fracture morphologies of Ti-8Al alloy fractured in alternate tension-compression fatigue: (a) Ti-8Al (heat treatment no. 1) fatigued at 500°C at a plastic strain amplitude of ±0.75%: (b) and (c) Ti-8Al (heat treatment no. 2) fatigued at 500°C at a plastic strain amplitude of ±0.5%.

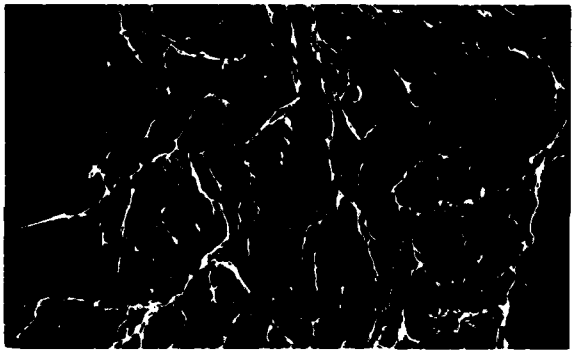

GP03-0954-71

Figure 46. Fracture morphology of Ti-8Al-0.1Y (heat treatment no. 1) fractured in alternate tension-compression at 500°C at a plastic strain amplitude of ±0.66%.

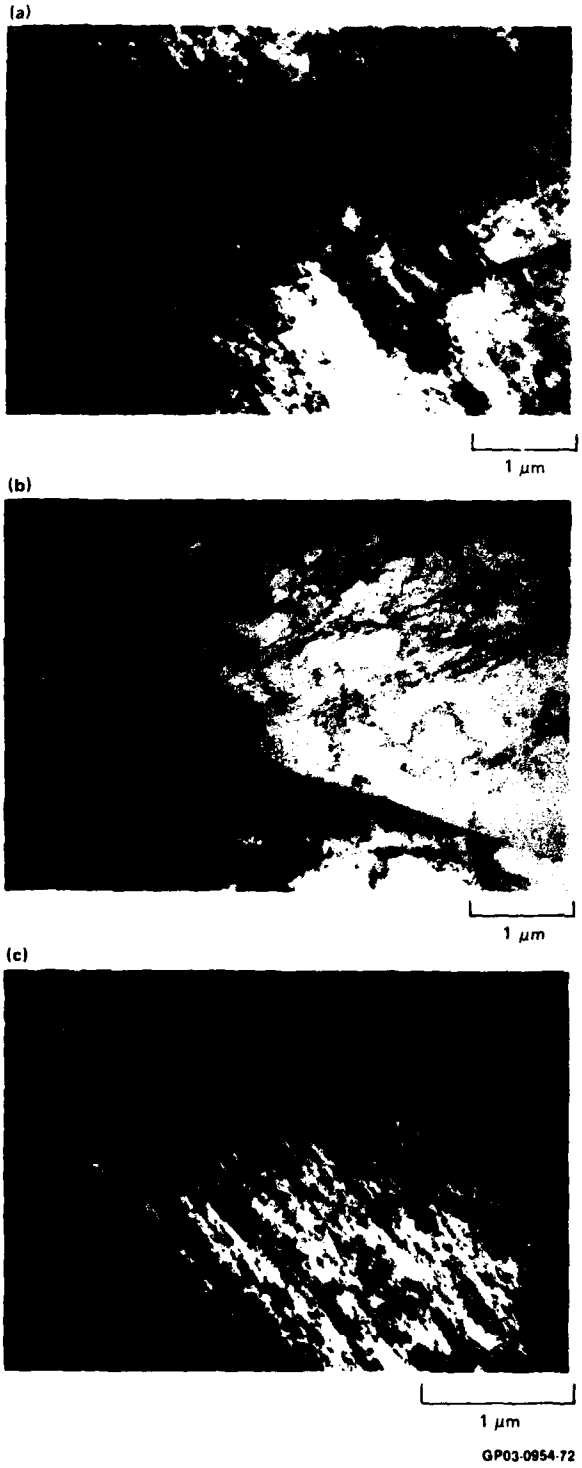

Figure 47. *Dislocation substructures in single-phase Ti-8Al* (heat treatment no. 1) deformed in alternate tension-compression at 500°C at a plastic strain amplitude of ± 0.75%.

Figure 48. Dislocation substructures in Ti-8Al-0.1Y (heat treatment no. 1) deformed in alternate compression at 25°C at a plastic strain amplitude of ± 0.66%.

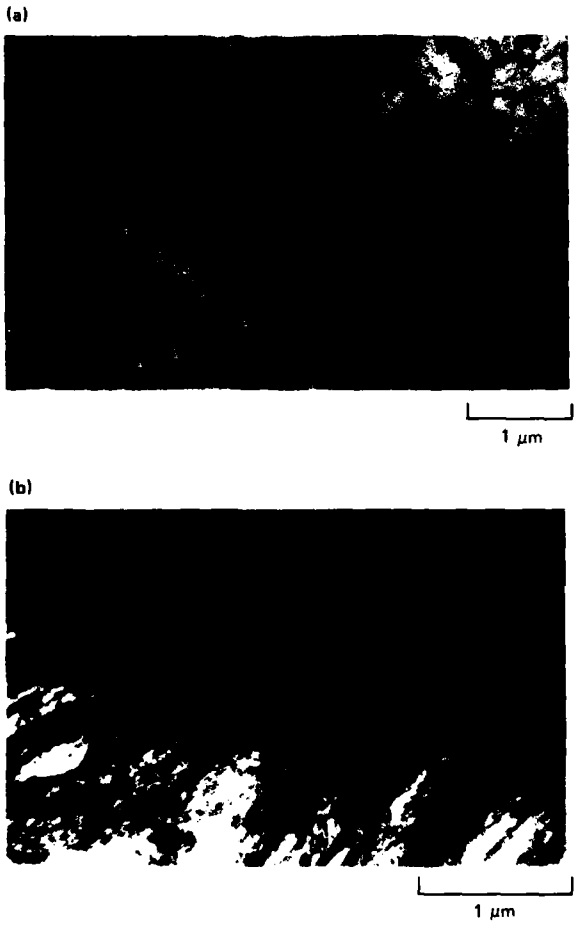

Figure 49. Dislocation substructures in Ti-8Al (heat treatment no. 2) deformed in alternate tension-compression at 500°C at a plastic strain amplitude of ± 0.5%.

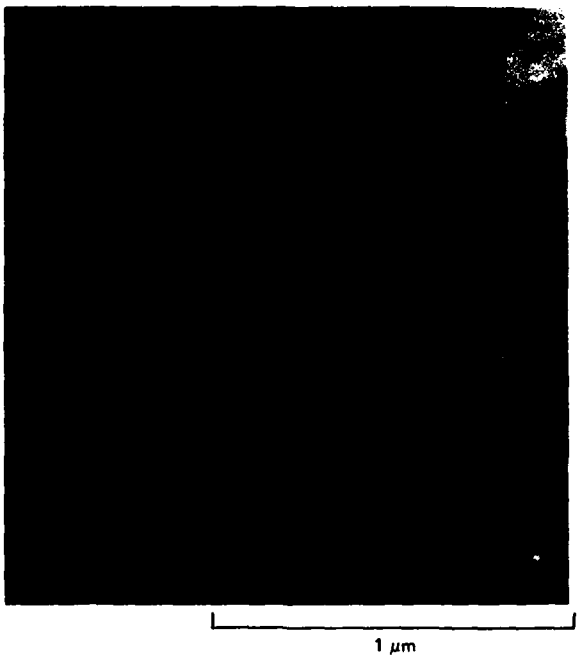

Figure 50. Deformation substructure in Ti-8Al (heat treatment no. 2) deformed in alternate tension-compression at 500°C at a plastic strain amplitude of ± 0.75%.

(a)

(b)

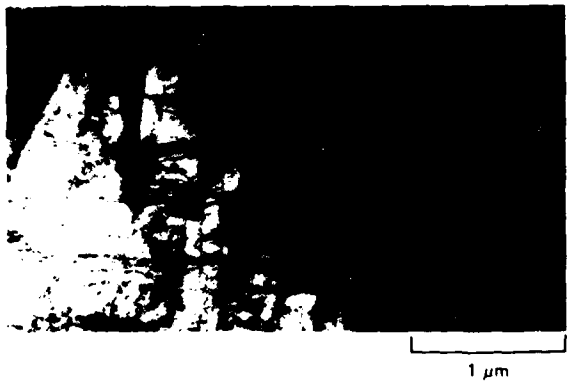

GP03-0954-74

Figure 51. Deformation substructures in Ti-8Al-0.2Er containing fine coherent α_2 precipitates (heat treatment no. 2) deformed in alternate tension-compression at 500°C at a plastic strain amplitude of ± 0.5%.

GP03-0954-75

Figure 52. Transmission of electron micrograph of precipitate/slip-band interactions in Ti-8Al-0.2Er deformed in alternate tension-compression fatigue at 500°C at a plastic strain amplitude of ±0.5%.

8. FRACTURE TOUGHNESS OF Ti-8Al-RE AND Ti-10Al-RE ALLOYS

The plane-strain fracture toughness, K_{Ic}, in the TL orientation was determined in accordance with ASTM Standard E399-74 for the Ti-8Al-RE alloys heat treated according to schedules shown in Table 10, and the results are summarized in Table 11. The dimensions of compact-tension specimens used for the study are shown in Figure 53. The Ti-8Al alloy aged at 600°C and containing α_2 precipitates has significantly lower fracture toughness than the single-phase alloy. The Y and Er additions result in a significant improvement in the fracture toughness of α_2-precipitation-strengthened Ti-8Al in the TL orientation.

TABLE 11. *PLANE-STRAIN FRACTURE TOUGHNESS (K_{Ic}) VALUES OF Ti-8Al-RE ALLOYS.*

Heat treatment*	Plane-strain fracture toughness, K_{Ic} (MPa $\sqrt{m}$)							
	Ti-8Al		Ti-8Al-0.05Y		Ti-8Al-0.1Y		Ti-8Al-0.2Er	
	L	T	L	T	L	T	L	T
600°C/500 h/AC to 25°C	25.2	44.3	45.0	48.4	39.3	43.9	–	42.0
950°C/30 min/AC to 25°C + 650°C/48 h/AC to 25°C	45.6	49.9	43.4	50.7	47.6	49.9	46.8	49.2
950°C/30 min/AC to 25°C	41.4	–	65.6	–	–	–	55.6	–

*AC = air cooled

GP03-0864-12

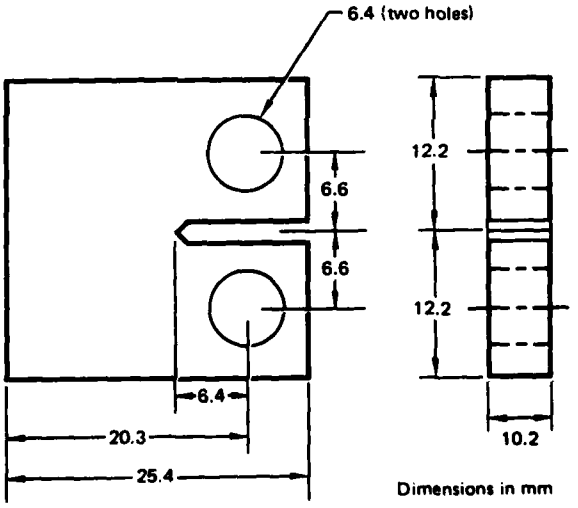

GP03-0854-79

Figure 53. Compact tension specimen for fracture toughness determination of Ti-8Al-RE and Ti-10Al-RE alloys.

9. CONCLUSIONS

Additions of up to 0.1 wt% Y and 0.2 wt% Er to Ti-8Al and Ti-10Al result in 50-200 nm diameter incoherent dispersoids. Higher amounts of Y and Er additions produce coarse 1-5 μm diameter particles.

The rare-earth-modified Ti-8Al alloys have considerably greater room-temperature ductility than standard Ti-8Al. The increased ductility arises from reduced planarity of slip resulting from interstitial-oxygen scavenging and dispersal of planar slip by the incoherent dispersoids.

Whereas the tensile and fatigue fractures in precipitation-strengthened Ti-8Al and Ti-10Al alloys occur predominantly by cleavage, fracture occurs by mixed cleavage and microvoid-coalescence in the Er- and Y-containing Ti-8Al alloys.

The creep rates at 400-600°C are significantly lower in Ti-8Al and Ti-10Al alloys than in Ti-6Al-4V. The presence of α_2 reduces the creep rates in Ti-8Al and Ti-10Al alloys, but the Y and Er additions do not alter the creep rates, stress exponents, and activation energies. The coherent α_2 precipitates increase the saturation and fracture stresses, produce fatigue softening, and reduce the low-cycle fatigue life of Ti-8Al and Ti-10Al alloys, but the Er and Y additions increase the low-cycle fatigue life. The Y and Er additions increase the plane-strain fracture toughness in the TL orientation of α_2-precipitation-strengthened Ti-8Al.

REFERENCES

1. C. R. Whitsett, S. M. L. Sastry, J. E. O'Neal, and R. J. Lederich, Influence of Rare-Earth Additions on Properties of Titanium Alloys: Microstructures and Room-Temperature Tensile Properties of Ti-6Al-4V with Yttrium, Erbium, and Mischmetal Additions, McDonnell Douglas Report MDC Q0627 (31 May 1977), Technical Report, ONR Contract No. N00014-76-C-0626.
2. C. R. Whitsett, S. M. L. Sastry, J. E. O'Neal, and R. J. Lederich, Influence of Rare-Earth Additions on Properties of Titanium Alloys: Room-Temperature Tensile Properties and Fracture Toughness of Ti-6Al-4V with Erbium, Yttrium, and Yttria Additions, McDonnell Douglas Report MDC Q0654 (31 May 1978), Technical Report, ONR Contract No. N00014-76-C-0626.
3. S. M. L. Sastry, R. J. Lederich, P. S. Pao, and J. E. O'Neal, Influence of Rare-Earth Additions on Properties of Titanium Alloys: Plane-Strain Fracture Toughness, Creep, and High-Temperature Deformation of Ti-6Al-4V with Erbium and Yttrium Additions, McDonnell Douglas Report MDC Q0684 (31 May 1979), Technical Report, ONR Contract No. N00014-76-C-0626.
4. M. J. Blackburn, The Ordering Transformations in Titanium-Aluminum Alloys Containing up to 25 at. pct. Aluminum, Trans. AIME 239, 1200 (1967).
5. J. C. Williams and M. J. Blackburn, The Structure, Mechanical Properties and Deformation Behavior of Ti-Al and Ti-Al-X Alloys, In Ordered Alloys: Structural Applications and Physical Metallurgy, ed. by B. H. Kear, C. T. Sims, N. S. Stoloff, and J. H. Westbrook (Claitors Publ. Div., Baton Rouge, LA, 1970), p. 425.
6. G. Lütjering and S. Wassman, Mechanical Properties of Age Hardened Titanium-Aluminum Alloys, Acta Met. 18, 785 (1970).
7. M. G. Mendiratta, Tensile Properties to 650°C and Deformation Structures in a Precipitation-Strengthened Titanium-Aluminum Alloy, NASA Technical Note TN D-7325 (June 1973).
8. H. Glieiter and E. Hornbogen, Precipitation Hardening by Coherent Particles, Mat. Sci. Eng. 2, 285 (1967/68).
9. M. G. Mendiratta, S. M. L. Sastry, and J. V. Smith, Effect of Grain Size Upon Flow and Fracture in a Precipitation-Strengthened Ti-8w/oAl-0.25w/oSi Alloy, J. Mat. Sci. 11, 1835 (1976).

10. B. B. Rath, J. E. O'Neal, and R. J. Lederich, Grain Refinement in Ti-Er Alloys, In Proc. EMSA, ed. by C. J. Arceneaux (Claitors Publ. Div., Baton Rouge, LA, 1974), p. 522.
11. B. B. Rath, R. J. Lederich, and J. E. O'Neal, The Effects of Rare-Earth Additions on the Grain Refinement of Ti, In Proc. 4th Bolton Landing Conf. on Grain Boundaries in Engineering Materials, ed. by J. L. Walter, J. H. Westbrook, and D. A. Woodford (Claitors Publ. Div., Baton Rouge, LA, 1975), p. 39.
12. M. F. Ashby, On the Orowan Stress, In Physics of Strength and Plasticity, ed. by A. S. Argon (M.I.T. Press, Cambridge, MA, 1969), p. 113.
13. P. B. Hirsch and J. F. Humphreys, Plastic Deformation of Two-Phase Alloys Containing Small Nondeformable Particles, In Physics of Strength and Plasticity, ed. by A. S. Argon (M.I.T. Press, Cambridge, MA, 1969), p. 189.

	Copies
Naval Sea System Command Washington, D.C. 20362 Attn: Code 035	1
Naval Facilities Engineering Command Alexandria, VA 22331 Attn: Code 03	1
Scientific Advisor Commandant of the Marine Corps Washington, D.C. 20380 Attn: Code AX	1
Naval Ship Engineering Center Department of the Navy Washington, D.C. 20360 Attn: Code 6101	1
Army Research Office P.O. Box 12211 Triangle Park, NC 27709 Attn: Metallurgy & Ceramics Program	1
Army Materials and Mechanics Research Center Watertown, MA 02172 Attn: Research Programs Office	1
Air Force Office of Scientific Research Bldg. 410 Bolling Air Force Base Washington, D.C. 20332 Attn: Chemical Science Directorate	1
Electronics & Solid State Sciences Directorate	1
Air Force Materials Laboratory Wright-Patterson AFB Dayton, OH 45433	1
Library Building 50, Rm 134 Lawrence Radiation Laboratory Berkeley, CA	1

	Copies
NASA Headquarters Washington, D.C. 20546 Attn: Code RRM	1
NASA Lewis Research Center 21000 Brookpark Road Cleveland, OH 44135 Attn: Library	1
National Bureau of Standards Washington, D.C. 20234 Attn: Metallurgy Division	1
Inorganic Materials Div.	1
Director Applied Physics Laboratory University of Washington 1013 Northeast Forthieth Street Seattle, WA 98105	1
Dèfense Metals and Ceramics Information Center Battelle Memorial Institute 505 King Avenue Columbus, OH 43201	1
Metals and Ceramics Division Oak Ridge National Laboratory P.O. Box X Oak Ridge, TN 37380	1
Los Alamos Scientific Laboratory P.O. Box 1663 Los Alamos, NM 87544 Attn: Report Librarian	1
Argonne National Laboratory Metallurgy Division P.O. Box 229 Lemont, IL 60439	1
Brookhaven National Laboratory Technical Information Division Upton, Long Island New York 11973 Attn: Research Library	1
Office Of Naval Research Branch Office 1030 East Green Street Pasadena, CA 91106	1

	Copies
Professor J. W. Morris, Jr. University of California College of Engineering Berkeley, CA 94720	1
Dr. Neil E. Paton Rockwell International Science Center 1049 Camino Dos Rios P.O. Box 1085 Thousand Oaks, CA 91360	1
Mr. A. Pollack Naval Ships R&D Center Code 2821 Annapolsi, MD 21402	1
Professor W. F. Savage Rensselaer Polytechnic Institute School of Engineering Troy, New York 02181	1
Professor O. D. Sherby Stanford University Materials Sciences Division Stanford, CA 94300	1
Dr. G. Ecer Westinghouse Electric Corporation Research & Development Center Pittsburgh, PA 15235	1
Dr. E. A. Starke, Jr. Georgia Institute of Technology School of Chemical Engineering Atlanta, GA 30332	1
Professor David Turnbull Harvard University Division Engineering and Applied Physics Cambridge, MA 02138	1
Dr. F. E. Wawner University of Virginia School of Engineering and Applied Science Charlottesville, VA 22901	1
Dr. C. R. Whitsett McDonnell Douglas Research McDonnell Douglas Corporation Saint Louis, MO 63166	1
Dr. J. C. Williams Carnegie-Mellon University Department of Metallurgy and Materials Sciences Schenley Park Pittsburgh, PA 15213	1
Professor H. G. F. Wilsdorf University of Virginia School of Engineering and Applied Sciences Charlottesville, VA 22903	1
Professor R. Mehrabian University of Illinois at Urbana-Champaign 144 Mechanical Engineering Building Urbana, IL 61801	1
Dr. N. J. Grant Massachusetts Institute of Technology Department of Materials Science and Engineering Cambridge, MA 02139	1
Professor P. R. Strutt University of Connecticut School of Engineering Department of Metallurgy Storrs, CT 06268	1
Mr. I. Caplan David W. Taylor Naval Ship Research and Development Center Code 2813 Annapolis, MD 21402	1
Dr. G. R. Leverant Southwest Research Institute 3500 Culebra Road P.O. Box 28610 San Antonio, TX 78284	1

DISTRIBUTION

	Copies
Defense Documentation Center Cameron Station Alexandria, VA 22314	12
Office of Naval Research Department of the Navy 800 N. Quincy Street Arlington, VA 22217	
Attn: Code 471	1
Code 102	1
Code 470	1
Commanding Officer Office of Naval Research Branch Office Building 114, Section D 666 Summer Street Boston, MA 02210	1
Commanding Officer Office of Naval Research Branch Office 536 South Clark Street Chicago, IL 60605	1
Office of Naval Research San Francisco Area Office One Hallidie Plaza Suite 601 San Francisco, CA 94102	1
Naval Research Laboratory Washington, D. C. 20375	
Attn: Code 6000	1
6100	1
6300	1
6400	1
2627	1
Naval Air Development Center Code 302 Warminster, PA 18964	
Attn: Mr. F. S. Williams	1
Naval Air Propulsion Test Center Trenton, NJ 08628	1
Attn: Library	1

	Copies
Naval Construction Batallion Civil Engineering Laboratory Port Hueneme, CA 93043	
Attn: Materials Division	1
Naval Electronics Laboratory San Diego, CA 92152	
Attn: Electron Materials Sciences Division	1
Naval Missile Center Materials Consultant Code 3312-1 Point Mugu, CA 92041	1
Commanding Officer Naval Surface Weapons Center White Oak Laboratory Silver Spring, MD 20910	
Attn: Library	1
David W. Taylor Naval Ship R&D Center Materials Department Annapolis, MD 21402	1
Naval Undersea Center San Diego, CA 92132	
Attn: Library	1
Naval Underwater System Center Newport, RI 02840	
Attn: Library	1
Naval Weapons Center China Lake, CA 93555	
Attn: Library	1
Naval Postgraduate School Monterey, CA 93940	
Attn: Mechanical Engineering Department	1
Naval Air Systems Command Washington, D.C. 20360	
Attn: Code 52031	1
52032	1

	Copies
Professor G. S. Ansell Rensselaer Polytechnic Institute Dept. of Metallurgical Engineering Troy, NY 02181	1
Professor H. K. Birnbaum University of Illinois Department of Metallurgy Urbana, IL 61801	1
Dr. E. M. Breinan United Technology Corporation United Technology Research Laboratories East Hartford, CT 06108	1
Professor H. D. Brody University of Pittsburgh School of Engineering Pittsburgh, PA 15213	1
Mr. R. Morante General Dynamics Electric Boat Division Eastern Point Road Groton, CT 06340	1
Professor J. B. Cohen Northwestern University Dept. of Material Sciences Evanston, IL 60201	1
Professor M. Cohen Massachusetts Institute of Technology Department of Metallurgy Cambridge, MA 02139	1
Professor Thomas W. Eager Massachusetts Institute of Technology Department of Materials Science and Engineering Cambridge, MA 02139	1
Professor B. C. Giessen Northeastern University Department of Chemistry Boston, MA 02115	1
Professor D. G. Howden Ohio State University Dept. of Welding Engineering 190 West 19th Avenue Columbus, OH 43210	1
Dr. C. S. Kortovich Dr. C. S. Kortovich TRW, Inc. 23555 Euclid Avenue Cleveland, OH 44117	1
Professor D. A. Koss Michigan Technological University College of Metallurgical Engineering Houghton, MI 49931	1
Professor A. Lawley Drexel University Dept. of Metallurgical Engineering Philadelphia, PA 19104	1
Professor Harris Marcus The University of Texas at Austin College of Engineering Austin, TX 78712	1
Dr. H. Margolin Polytechnic Institute of New York 333 Jay Street Brooklyn, NY 11201	1
Professor K. Masubuchi Massachusetts Institute of Technology Department of Ocean Engineering Cambridge, MA 02139	1